




Unique Actions of GABA Arising from Cytoplasmic Chloride Microdomains

 Negah Rahmati,^{1*} Kieran P. Normoyle,^{1*} Joseph Glykys,² Volodymyr I. Dzhalala,¹  Kyle P. Lillis,¹ Kristopher T. Kahle,³ Rehan Raiyyani,¹ Theju Jacob,¹ and  Kevin J. Staley¹

¹Department of Neurology, Harvard Medical School and Massachusetts General Hospital, Boston, Massachusetts 02114, ²Department of Pediatrics and Neurology, Iowa Neuroscience Institute, Carver College of Medicine, University of Iowa, Iowa City, Iowa 52242, and ³Departments of Neurosurgery, Pediatrics, and Cellular & Molecular Physiology, Yale School of Medicine, New Haven, Connecticut 06510

Developmental, cellular, and subcellular variations in the direction of neuronal Cl^- currents elicited by GABA_A receptor activation have been frequently reported. We found a corresponding variance in the GABA_A receptor reversal potential (E_{GABA}) for synapses originating from individual interneurons onto a single pyramidal cell. These findings suggest a similar heterogeneity in the cytoplasmic intracellular concentration of chloride ($[\text{Cl}^-]_i$) in individual dendrites. We determined $[\text{Cl}^-]_i$ in the murine hippocampus and cerebral cortex of both sexes by (1) two-photon imaging of the Cl^- -sensitive, ratiometric fluorescent protein SuperClomeleon; (2) Fluorescence Lifetime IMaging (FLIM) of the Cl^- -sensitive fluorophore MEQ (6-methoxy-*N*-ethylquinolinium); and (3) electrophysiological measurements of E_{GABA} by pressure application of GABA and RuBi-GABA uncaging. Fluorometric and electrophysiological estimates of local $[\text{Cl}^-]_i$ were highly correlated. $[\text{Cl}^-]_i$ microdomains persisted after pharmacological inhibition of cation–chloride cotransporters, but were progressively modified after inhibiting the polymerization of the anionic biopolymer actin. These methods collectively demonstrated stable $[\text{Cl}^-]_i$ microdomains in individual neurons *in vitro* and *in vivo* and the role of immobile anions in its stability. Our results highlight the existence of functionally significant neuronal Cl^- microdomains that modify the impact of GABAergic inputs.

Key words: chloride; chloride microdomains; GABA; GABA_A receptors; SuperClomeleon; FLIM

Significance Statement

Microdomains of varying chloride concentrations in the neuronal cytoplasm are a predictable consequence of the inhomogeneous distribution of anionic polymers such as actin, tubulin, and nucleic acids. Here, we demonstrate the existence and stability of these microdomains, as well as the consequence for GABAergic synaptic signaling: each interneuron produces a postsynaptic GABA_A response with a unique reversal potential. In individual hippocampal pyramidal cells, the range of GABA_A reversal potentials evoked by stimulating different interneurons was >20 mV. Some interneurons generated postsynaptic responses in pyramidal cells that reversed at potentials beyond what would be considered purely inhibitory. Cytoplasmic chloride microdomains enable each pyramidal cell to maintain a compendium of unique postsynaptic responses to the activity of individual interneurons.

Introduction

The group mean values of GABA_A receptor reversal potential (E_{GABA}) are continuously distributed over a 25 mV range from -85 to -60 mV in 20 recent studies using gramicidin perforated patch-recording techniques in CA1 pyramidal cells from rodents

with mature neuronal Cl^- transport (Romo-Parra et al., 2008; Tyzio et al., 2008; Table 1). There was no relationship between the number of observations and the value of E_{GABA} (Pearson's $r = -0.13$, $p = 0.5$), suggesting that physiological variance in E_{GABA} rather than inadequate sampling explains the range of results. Such variance could arise from intercellular variance in E_{GABA} or from intracellular (subcellular) variance. Over this wide range of reversal potentials, the effects of GABA_A receptor (GABA_AR)-gated currents will vary from inhibition via hyperpolarization of the membrane potential, through shunting inhibition, to excitation mediated by activation of low-threshold calcium currents and partial relief of the magnesium block of NMDA receptors (Doyon et al., 2016). These divergent effects suggest that E_{GABA} must be tightly regulated, although the mechanisms of regulation have not been resolved.

Received Dec. 18, 2020; revised Mar. 10, 2021; accepted Apr. 10, 2021.

N.R. and K.J.S. designed research; N.R., K.P.N., J.G., and V.I.D. performed research; N.R., K.P.N., K.P.L., R.R., and T.J. analyzed data; N.R., K.P.N., K.T.K., and K.J.S. wrote the paper.

K.J.S. was supported by National Institutes of Health (NIH)/National Institute of Neurological Disorders and Stroke (NINDS) Grant 5R01-NS-40109-14. J.G. was supported by NIH/NINDS Grant 1K08-NS-091248.

*N.R. and K.P.N. contributed equally to this work.

The authors declare no competing financial interests.

Correspondence should be addressed to Kevin J. Staley at staley.kevin@mgh.harvard.edu.

<https://doi.org/10.1523/JNEUROSCI.3175-20.2021>

Copyright © 2021 the authors

Table 1. Reported range of E_{GABA} in 20 published studies

Study	E_{GABA} (mV)	<i>N</i>	Technique	Citation	Notes
1	−89.0	6	Gramicidin	Nakahata et al., 2010	
2	−87.0	6	Gramicidin	Ormond and Woodin, 2009	
3	−82.7	17	Gramicidin	Ilie et al., 2012	
4	−81.2	6	Gramicidin	Galanopoulou, 2008	Female mice
5	−81.0	4	Cell attached	Chorin et al., 2011	
6	−79.0	12	Gramicidin	Pavolv et al., 2011	
7	−78.0	5	Gramicidin	Zhan et al., 2006	
8	−77.0	8	Gramicidin	Lagostena et al., 2010	
9	−75.8	6	Gramicidin	Tanaka et al., 1997	Evoked in SLM
10	−74.2	8	Gramicidin	Galanopoulou, 2008	Male mice
11	−74.0	18	Gramicidin	Tyzio et al., 2007	
12	−72.6	6	Gramicidin	Tanaka et al., 1997	Evoked in SP
13	−72.0	5	Cell attached	Tyzio et al., 2008	
14	−69.0	6	Gramicidin	Rieki et al., 2008	
15	−68.9	7	Gramicidin	Barmashenko et al., 2011	
16	−68.7	18	Gramicidin	Raimondo et al., 2012	
17	−68.0	9	Gramicidin	MacKenzie and Maguire, 2015	
18	−67.8	10	Gramicidin	Sauer et al., 2012	
19	−66.3	12	Gramicidin	Balena et al., 2010	
20	−56.6	6	Gramicidin	Yang et al., 2015	

Twenty group means of E_{GABA} measurements using gramicidin and cell-attached techniques in age-matched CA1 pyramidal cells. SP, Stratum pyramidale; SLM, stratum lacunosum-moleculare. The group mean values of E_{GABA} in 20 separate studies shown indicate a distribution >25 mV. The number of recorded cells (*N*) in each study varies between 4 and 18. There is no significant correlation between the number of recorded cells and the reported E_{GABA} values (Pearson's $r = -0.13$, $p = 0.5$) or the variation in E_{GABA} values indicated by the SEM (Pearson's $r = -0.38$, $p = 0.1$).

The observed range in E_{GABA} could be explained by a few millimolar variation in the cytoplasmic intracellular concentration of chloride ($[Cl^-]_i$), the anion with the highest permeability through GABA_ARs (Alfonso et al., 2015; Doyon et al., 2016; Raimondo et al., 2017). Such differences in $[Cl^-]_i$ could be maintained by the active transport of Cl^- . For example, KCC2 and NKCC1 are oppositely directed cation- Cl^- cotransporters (CCCs) expressed in neurons (Kahle et al., 2015). However, these are high-velocity transporters whose ionic equilibrium conditions do not match well with the distribution of observed E_{GABA} (Delpire and Staley, 2014), and neither acute (Glykys et al., 2014a; Sato et al., 2017) nor chronic (Goutierre et al., 2019) inhibition of transport produces the predicted changes in $[Cl^-]_i$ (i.e., a passive distribution that collapses the Cl^- driving force).

Another possibility is the well established partitioning effects on mobile ions exerted by the distribution of immobile ions (Fatin-Rouge et al., 2003) that, for example, create Gibbs-Donnan effects across semipermeable membranes (Donnan, 1911), in gels (Procter, 1914), and in unlinked biopolymers (Marinsky, 1985), and form the basis of ion exchange technologies such as water softening and ion exchange chromatography (Yamamoto et al., 1988; Helfferich, 1995). Relatively immobile cytoplasmic biopolymers with high and spatially inhomogeneous densities of anionic charge, such as actin, tubulin, and nucleic acids (Gianazza and Righetti, 1980; Sanabria et al., 2006; Janke et al., 2008; Chen et al., 2020) could displace Cl^- locally (Glykys et al., 2014a, 2017). Recent studies have underscored substantial variance in the subcellular distribution of these anionic biopolymers (Koleske, 2013; Morawski et al., 2015; Gut et al., 2018; Chen et al., 2020), suggesting that if the displacement of Cl^- underlies the intercellular diversity in E_{GABA} , there should be a corresponding spatial variance in the subcellular distribution of Cl^- . Indeed, many reports have suggested subcellular variance in $[Cl^-]_i$ or E_{GABA} (Pouzat and Marty, 1999; Berglund et al., 2006; Duebel et al., 2006; Szabadics et al., 2006; Romo-Parra et al., 2008; Földy et al., 2010; Glykys et al., 2014a; Astorga et al., 2015;

Untiet et al., 2016; Zorrilla de San Martin et al., 2017; Schmidt et al., 2018) for which several mechanisms have been proposed (Khirug et al., 2008; Földy et al., 2010; Glykys et al., 2014a).

We report a subcellular variance in E_{GABA} (Fig. 1) that fits the published range of E_{GABA} values summarized in Table 1, and we demonstrate a corresponding variance in local neuronal $[Cl^-]_i$ *in vivo* and *in vitro*. Several complimentary techniques were used including two-photon microscopy of the ratiometric Cl^- indicator SuperClomelon (sCLM; Grimley et al., 2013); Fluorescence Lifetime IMaging (FLIM) of Cl^- -sensitive, pH-insensitive dye 6-methoxy-*N*-ethylquinolinium (MEQ; Biwersi and Verkman, 1991); and simultaneous direct measurement of the reversal potential of locally activated GABA_A-gated membrane currents by puffing or uncaging GABA. We assessed the range, stability, transport dependence, and influence of anionic macromolecules on the observed variance in local baseline $[Cl^-]_i$. Our results highlight the existence of functionally significant neuronal Cl^- microdomains that modify the impact of GABAergic inputs.

Materials and Methods

Ethics statement

All experiments were performed in accordance with protocols approved by the Center for Comparative Medicine at Massachusetts General Hospital and in accordance with the National Institutes of Health *Guide for the Care and Use of Laboratory Animals*.

Mice

Construction of the sCLM targeting vector. The STK1-HR gene-targeting vector was constructed from 129Sv mouse genomic DNA (genOway). The final targeting vector has the following features: (1) isogenic with 129Sv ES cells, favoring the homologous recombination; (2) asymmetrical homology arms (5' short arm-SA: 1 kb, 3' long arm-LA: 4.3 kb); (3) transgenic cassette containing the sCLM-pA elements allowing the expression of the transgene under the control of the ubiquitous CAAG promoter sequences; (4) LoxP-flanked, combined STOP-neomycin selection (Neo) cassette allowing its excision through the action of Cre-recombinase, activating the sCLM overexpression; and (5) the presence of the diphtheria toxin A (DTA)-negative selection marker reduces the isolation of nonhomologous recombined embryonic stem (ES) cell clones (Fig. 2).

Production of sCLM targeted ES cell clones. Linearized targeting vector was transfected into 129Sv ES cells (genOway) according to genOway electroporation procedures. PCR, Southern blot, and sequence analysis of G-418-resistant ES cell clones revealed the recombined locus in two clones. PCR across the 5' end of the targeted locus used a forward primer hybridizing upstream of the 5' homology arm (5'-AAGACG AAAAGGGCAAGCATCTTCC-3') and a reverse primer hybridizing within the neomycin cassette (5'-GCAGTGAGAAGAGTACCACC AAGAGTCC-3'). Two Southern blot assays were hybridized with an internal and an external probe to assess recombination accuracy at the respective 5' and 3' ends of the sCLM locus. The absence of off-target mutations was confirmed by sequence analysis.

Generation of chimeric mice and breeding scheme. Recombined ES cell clones microinjected into C57BL/6 blastocysts gave rise to male chimeras with statistically significant ES cell contribution. These chimeras were bred with C57BL/6J mice expressing Cre recombinase to produce the sCLM heterozygous line lacking the neomycin cassette. F1 genotyping was performed by PCR and Southern blot. PCR primers hybridizing upstream (5'-GGGCAACGTGCTGGTTATTGTGC-3') and downstream (5'-ACAGTCTCCTGCCCTTGCTCAC-3') of the neomycin cassette allowed PCR identification of the 3195 bp sCLM allele amplicon harboring the neomycin cassette, and the 177 bp amplicon lacking the neomycin cassette. Southern blot hybridization with an external probe allowed identification of the 3.7 kb sCLM allele (Fig. 2B,C).

Ratiometric $[Cl^-]_i$ measurements were performed on strain 129 sCLM mice (Grimley et al., 2013) by crossing sCLM-floxed mice with C57BL/6 Synapsin-Cre (for neuronal expression) or C57BL/6 DLX-Cre

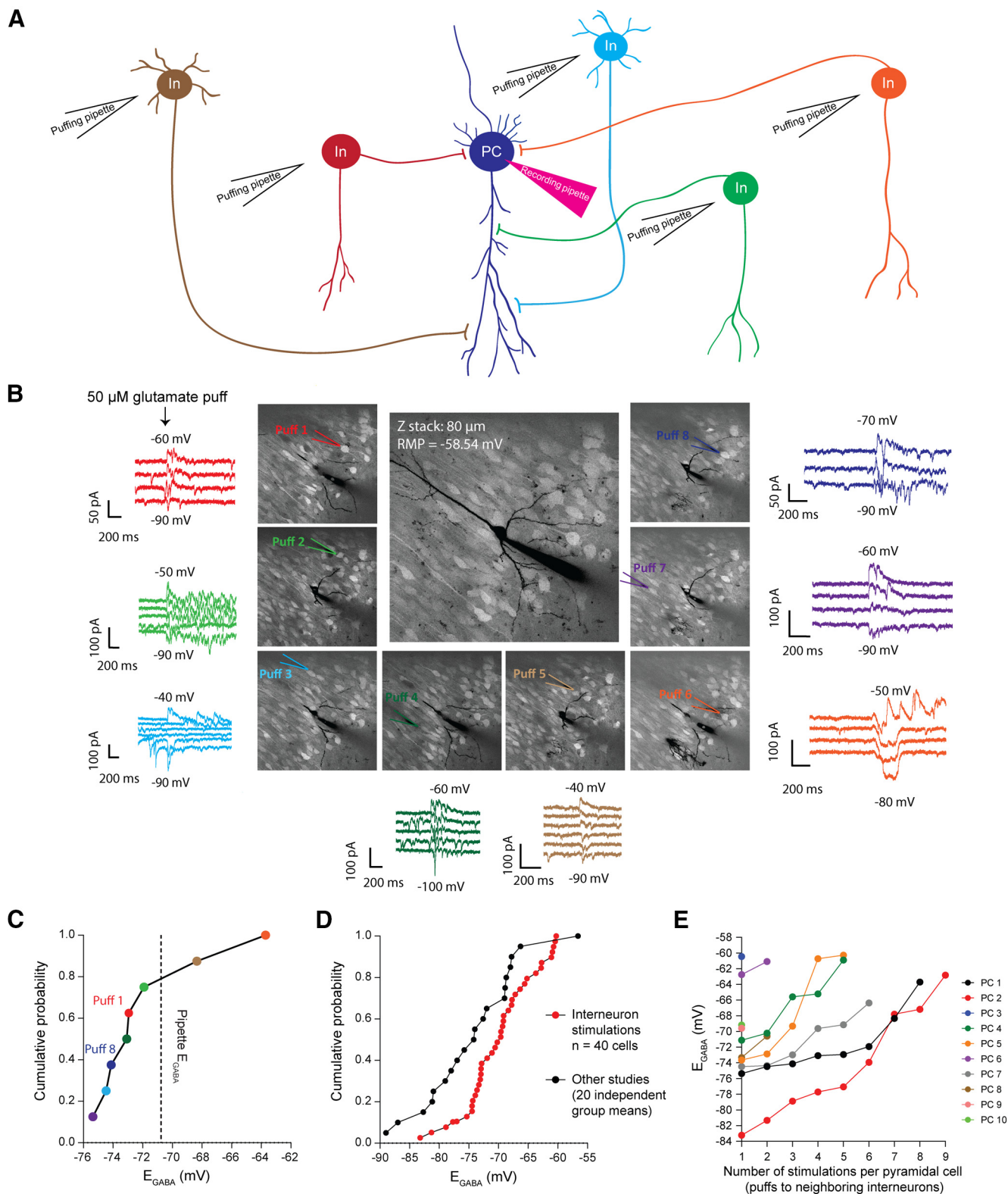
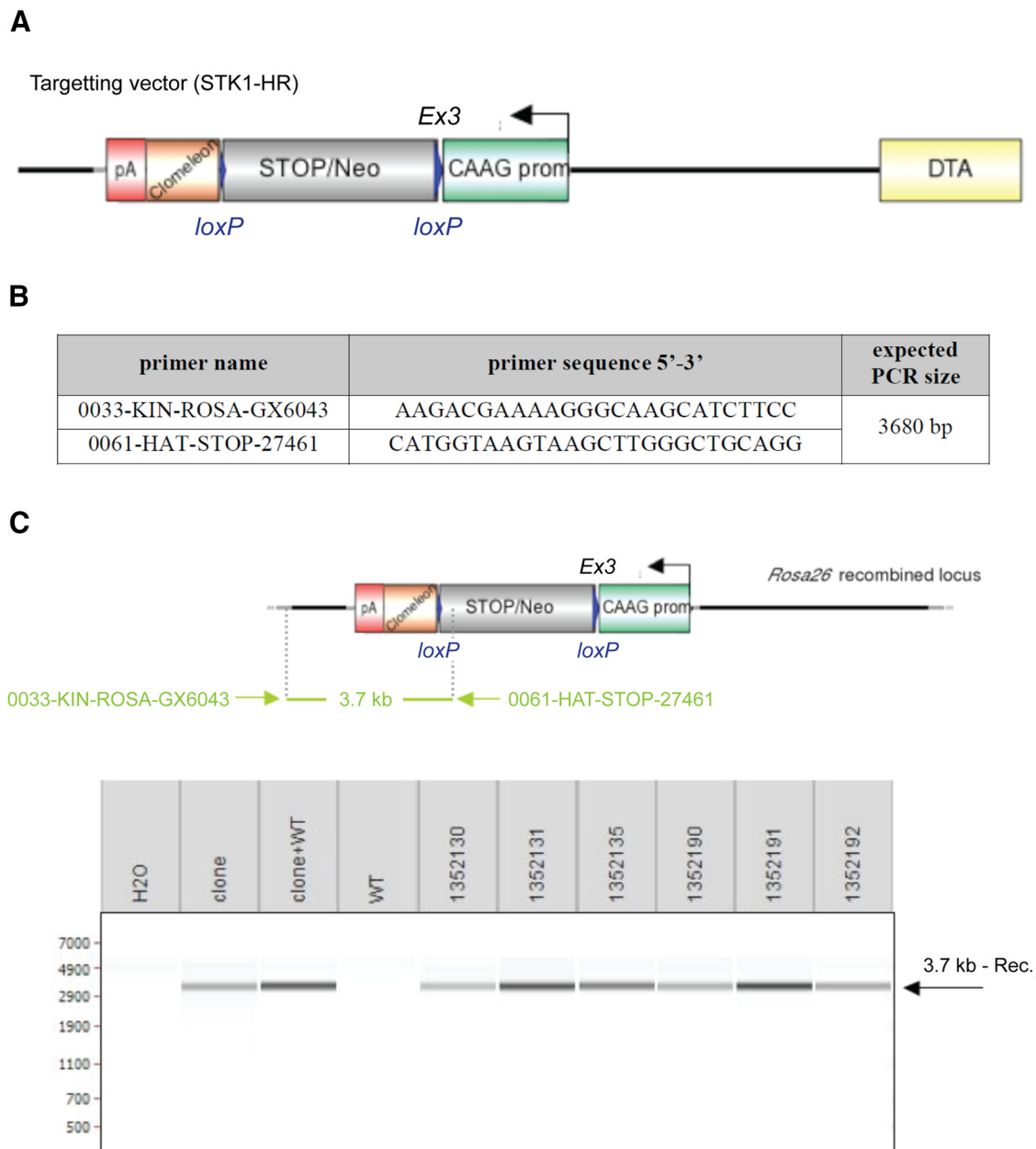


Figure 1. Inhomogeneity in responses to GABAergic interneurons. **A**, An illustration of the designed experiment to test for inhomogeneity of GABAergic signaling in single pyramidal cells (PCs). The pyramidal cell is recorded by whole-cell patch-clamp technique. Neighboring interneurons (In) are stimulated separately by puffing 50 μM glutamate to their cell bodies. Stimulation of those interneurons that are presynaptic to the recorded pyramidal cell evokes GABAergic currents. This is a simplified illustration. In reality, each interneuron makes multiple synapses to the target pyramidal cell. Therefore, the variance of E_{GABA} at individual synapses may be higher. **B**, An example of a recorded pyramidal cell and the stimulated neighboring interneurons (labeled with tdTomato) and the evoked GABA currents with different reversal potentials. **C**, Range of E_{GABA} measured in **B**. The colors of data points in **C** match the colors of traces and puff pipettes in **B**. The black dashed line shows the calculated E_{GABA} based on the Cl^- concentration inside the recording pipette (pipette E_{GABA}). The puffing pipette was manually returned to the same area by the end of the experiment (puff 1 and puff 8 in **B**). The difference between the E_{GABA} evoked by puff 1 and that by puff 8 was <2 mV, while the time interval between these two puffs was ~ 50 min. Although puff 8 was applied later than puff 1, its evoked E_{GABA} value was farther away from the pipette E_{GABA} compared with that from puff 1. These findings argue against the possibility that the $[\text{Cl}^-]$ inside the recording pipette homogenizes the dendritic $[\text{Cl}^-]$. **D**, Summary of our experiments ($n = 40$ cells) and 20 separate studies (indicated in Table 1) indicating a



(for interneuron expression). FLIM experiments were performed on C57BL/6 wild-type (WT) mice. Functional studies of $[Cl^-]_i$ microdomains were performed on DLX-Cre mice to visualize interneurons. Either sex was used for experiments.

←

wide range in E_{GABA} values in age-matched CA1 pyramidal cells. **E**, Ten pyramidal cells were included in these experiments. One or several interneurons around each of those PCs were stimulated (in total, 40 connected interneurons). In some experiments, only one or two series of stimulations of neighboring interneurons per pyramidal cell could be completed while the passive properties of the patched pyramidal cells remained stable. The number of stimulations (puffs) was not significantly correlated with the variance in E_{GABA} (Pearson's $r = 0.66$, $p = 0.1$).

In vivo imaging. Craniectomies were performed under aseptic conditions, under anesthesia with inhaled isoflurane, and in a stereotaxic frame. The temperature was regulated through a heating pad. The surgical site was sterilized with betadine and isopropyl alcohol, and a 2–3 mm incision was made in the scalp along the midline between the ears. A 5- to 7-mm-diameter hole was drilled in the skull, 1 mm lateral, and posterior to bregma (parietal region) using a high-speed microdrill. Once the craniotomy was completed, a thin round coverglass (~100 μ m) was secured to the bone with a mixture of superglue and dental cement. Immediately after the craniotomy, the mice were imaged under the two-photon microscope while maintaining anesthesia and normo-temperature.

Organotypic hippocampal slice preparation. Postnatal day 6 (P6) to P7 mice were used to prepare organotypic slice cultures using the rocking plate technique (Romijn et al., 1988) or the membrane insert

technique (Stoppini et al., 1991) for electrophysiology and imaging. Isolated hippocampi were cut into 400 μm slices on a McIlwain tissue chopper (Mickle Laboratory Engineering). Slices were transferred to membrane inserts (PICMORG50, Millipore) or coverslips, which were placed in glass-bottomed six-well plates (catalog #P06-1.5H-N, CellVis). Both culture configurations were incubated at 5% CO_2 , 36°C in Neurobasal-A growth medium supplemented with 2% B27, 500 μM GlutaMAX, and 0.03 mg/ml gentamycin (all from Thermo Fisher Scientific). The growth medium was changed every 3–4 d. Slices were used for experiments between day *in vitro* (DIV) 6 and DIV 20.

Dissociated cell culture preparation. Hippocampal murine neurons were prepared based on the method of Beaudoin et al. (2012), modified to use early postnatal mice, and to use a commercial kit (LK003150, Worthington Biochemical). P1–P4 mice were killed by guillotine method cut just caudal to the ears. Bilateral incisions were made from ear to eye as far ventral as feasible, allowing rostral reflection of the calvaria. Using a spatula dipped in Gey's Balanced Salt Solution (GBSS; catalog #G9779, Sigma-Aldrich) supplemented with glucose (Sigma-Aldrich) to 1.5% and then filter sterilized, brains from up to four animals were gently removed to a 6 cm Petri dish of glucose-supplemented GBSS in 6 cm Petri dish on ice. Each hippocampus was dissected out and transferred to a second 6 cm Petri dish of glucose-supplemented GBSS on a cold pack within the preparation hood. Using a commercially available papain tissue dissociation kit (catalog #LK003150, Worthington Biochemical), hippocampi were transferred to Earle's Balanced Salt Solution (EBSS)-based papain solution supplemented with DNase in a 6 cm Petri dish pre-equilibrated in 5% CO_2 36°C incubator and chopped for 30 s with Bonn scissors before being returned to incubator for a 10- to 40 min incubation commensurate with pup age. Halfway through incubation, tissue was triturated 5 \times with a 10 ml plastic pipette and returned to the incubator. Reduced yield from using plastic pipettes was deemed acceptable to avoid inconsistency of flame-polished glass tip diameter and subsequent trituration-related damage. Tissue was again triturated 5 \times with a 10 ml pipette and 3–4 \times with a 5 ml pipette before being strained through a 40 μm basket filter (catalog #431750, Corning) and transferred to a 50 ml conical tube. The cell mixture was centrifuged for 6 min at 300 \times g, and after carefully aspirating the supernatant the cell pellet was then resuspended with EBSS plus an ovomucoid inhibitor albumin mixture supplemented with DNase (each part of the Worthington Biochemical dissociation kit). Gentle trituration with a 10 ml pipette held several centimeters from the tube bottom was sufficient to resuspend. This mixture was then carefully and slowly overlaid atop 5 ml of ovomucoid protein in EBSS and centrifuged for 5 min at 70 \times g. The resulting pellet was resuspended in Neurobasal-A media (catalog #10888-022, Thermo Fisher Scientific) without supplementation and transferred to a fresh tube. The cell concentration and proportion surviving were calculated using Trypan Blue and a hemocytometer, and preplated to poly-D-lysine- and laminin-coated (catalog #P0899 and laminin L2020, respectively, Sigma-Aldrich) 19 mm coverslips (Electron Microscopy Services) or gridded glass-bottom 3.5 cm Petri dishes (catalog #81168, ibidi) delivering 300 viable neurons/ mm^2 at overall amounts between 2 \times 10⁵ and 5 \times 10⁵ cells in the absence of media supplementation. After a preplating period of 2 h during which neurons preferentially attached to the coated surface, unattached cells were aspirated, and fresh Neurobasal-A media supplemented as described above (Organotypic Hippocampal Slice Preparation). Fresh media replaced half of the full volume every 2–3 d. Neurons were imaged between DIV 10 and DIV 20.

Chloride measurements

We used the following three methods to measure $[\text{Cl}^-]_i$.

Two-photon sCLM imaging. The sCLM (Grimley et al., 2013) variant of Clomeleon (CLM; Kuner and Augustine, 2000) was used for noninvasive $[\text{Cl}^-]_i$ imaging. sCLM consists of two fluorescent proteins CFP (cyan fluorescent protein) and YFP (yellow fluorescent protein), joined by a short polypeptide linker, which allows FRET-based imaging of $[\text{Cl}^-]_i$ (Grimley et al., 2013). For the Cl^- imaging experiments performed without electrophysiological recordings, two-photon imaging was performed using a FluoView 1000MPE microscope with prechirp optics and a fast

acousto-optical modulator mounted on an Olympus BX61W1 upright microscope equipped with a 25 \times 1.05 numerical aperture (NA) water-immersion objective (Olympus). A mode-locked Ti:Sapphire laser (MaiTai, Spectra-Physics) generated two-photon fluorescence with 860 nm excitation. Emitted light was detected through two filters in the range of 460–500 nm for CFP and 520–560 nm for YFP. Two photomultiplier tubes (Hamamatsu Photonics) were used to acquire CFP and YFP signals simultaneously. Three-dimensional stacks (3D) of raster scans in the x - y plane (0.33 $\mu\text{m}/\text{pixel}$ x - y) were imaged at a z -axis interval of 1 μm for measuring the stability of microdomains (see Figs. 8, 9) and a z -axis interval of 2 μm for the rest of experiments. The pyramidal cell shown (see Fig. 4E,F) was imaged with a higher resolution (0.099 $\mu\text{m}/\text{pixel}$ x - y and a z -axis interval of 1 μm). Simultaneous two-photon and electrophysiological recordings were performed with a custom-built scanning microscope. Two-photon images were acquired using custom-designed software (LabVIEW) and a scan head from Radiance 2000 MP (Bio-Rad), equipped with a 40 \times , 0.8 NA water-immersion objective (Olympus), and photomultiplier tubes with appropriate filters for CFP (450/80) and YFP (545/30). A Spectra-Physics Mai Tai laser was set to 860 nm for sCLM imaging. Serial images were collected with a z -axis interval of 2 μm . The images were reconstructed offline either by ImageJ (RRID:SCR_003070) or MATLAB (version 2017a). To calculate $[\text{Cl}^-]_i$ using ImageJ, a region of interest (ROI) was drawn around the cell body and dendrites, and the ratio of YFP/CFP fluorescence intensity was measured. Images analyzed with MATLAB were masked using image processing functions as described below. In either case, the ratio was converted into $[\text{Cl}^-]_i$ by the following equation:

$$[\text{Cl}^-]_i = K_d \frac{(R_{\text{max}} - R)}{(R - R_{\text{min}})},$$

where K_d is the dissociation constant, R_{max} is the ratio obtained in the absence of Cl^- , and R_{min} is the ratio when sCLM is maximally quenched (Grimley et al., 2013; see Fig. 4A).

FLIM of MEQ. MEQ, 1.5 mM, was delivered to the cytoplasm via whole-cell recording pipette (see Fig. 7F). Unlike sCLM, MEQ is insensitive to pH (Biversi et al., 1992). The Cl^- -sensitive signals of both fluorophores used in this study are independent of the dye concentration due to either the ratiometric nature of sCLM fluorescence or the intrinsic nature of fluorescence lifetime as a property of MEQ that is independent of fluorophore concentration. MEQ was excited at 750 nm using the custom-built scanning microscope detailed above with an appropriate emission filter (390/65), and fluorescence lifetime was measured using SPCLImage software (Becker & Hickl). The selection of the ROI and calculation of the MEQ lifetime was measured offline by a custom-written MATLAB (MathWorks) program. MEQ lifetime values were translated to $[\text{Cl}^-]_i$ using the Stern–Volmer calibration (see Fig. 4B; Biversi et al., 1992). The detailed morphologies of the cells were visualized by adding 20 μM Alexa Fluor-594 to the recording pipette. High-resolution Alexa Fluor-594 images (x - y axis, 0.307 $\mu\text{m}/\text{pixel}$; z -axis, 2 $\mu\text{m}/\text{pixel}$) were used for precise selection of the ROI in MEQ lifetime images with x - y resolution of 1.537 $\mu\text{m}/\text{pixel}$ and z -axis interval of 2 μm .

Electrophysiological measurement of E_{GABA} . A subset of experiments was performed using whole-cell and gramicidin perforated patch-clamp techniques (for details, see Electrophysiology section) in conjunction with sCLM imaging or FLIM. The E_{GABA} was extracted from the intercept of currents evoked by the application of 10 μM GABA applied via a micropipette and driven by a 10 ms, 5 psi square-wave pressure transient (Picospritzer III, General Valve) to visualized segments of the dendrites while clamping the cell at voltage steps ranging from -110 to $+10$ mV. GABA_BRs were blocked by 2 μM CGP55845. The size of the dendritic region of interest was determined by adding Alexa Fluor-594 inside the puffing pipette and measuring the region over which the dye diffused. $[\text{Cl}^-]_i$ was calculated using the Nernst equation, as follows:

$$E_{\text{Cl}} = -\frac{RT}{F} \times \ln \frac{[\text{Cl}^-]_o}{[\text{Cl}^-]_i}$$

where R is the gas constant (8.315 J/mol/K), T is the temperature in Kelvin, F is the Faraday's constant (96.487 C/mol), and $[\text{Cl}^-]_o$ is the extracellular concentration of chloride.

Electrophysiology

For electrophysiological recordings, organotypic slice cultures or dissociated cultured cells were transferred to a recording chamber and perfused with ACSF (2.5 ml/min) containing the following (in mM): 124 NaCl, 1.25 NaH₂PO₄, 2.5 KCl, 26 NaHCO₃, 2 CaCl₂, 2 MgSO₄, and 20 D-glucose, bubbled with 95% O₂ and 5% CO₂ at 34°C. The following two separate series of electrophysiological experiments were performed. The first was gramicidin perforated patch clamping on hippocampal dissociated cell cultures, where cells were visualized using an upright microscope (Eclipse FN1, Nikon) equipped with a 40×, 0.8 NA water-immersion objective (Nikon), a DualView image intensifier (Optical Insights), and a CCD camera (Chameleon3, Point Gray Research) for simultaneous acquisition of two separate images of CFP and YFP with *x* resolution of 1.996 μm/pixel and *y* resolution of 1.896 μm/pixel (see Fig. 7A). Electrodes were pulled from borosilicate glass capillaries (Sutter Instruments) using a micropipette puller (model P-97, Sutter Instruments) with resistance of 5–7 MΩ when filled with internal solution containing the following (in mM): 140 KCl, 5 MgCl₂, 10 HEPES, and 5 EGTA, with osmolarity of 290 mOsm, pH 7.25–7.35, adjusted with KOH. Gramicidin perforated patch clamping was performed as described previously (Rahmati et al., 2016). Primary dendrites of sCLM cells were selected as ROIs to have a higher resolution and signal-to-noise ratio. The second was whole-cell patch-clamp recording of hippocampal organotypic slices: these experiments were performed on wild-type C57 rocking plate organotypic slices to simultaneously load the hippocampal pyramidal cells with MEQ for FLIM imaging and measure E_{GABA} at different segments of the dendrites by 50 μM GABA puff application (see Fig. 7F,G). Whole-cell patch-clamp recordings were also performed for functional evaluation of Cl⁻ microdomains (Fig. 1) on organotypic slices of DLX-Cre mice, which were transfected on the day of slicing with tdTomato virus (Addgene-AAV9-CAG-FLEX-tdTomato, in 2 μl/ml culture media) to visualize interneurons. Whole-cell recordings were used to improve the stability of this complex experiment, which involved repeated current–voltage measurements over a wide range of membrane potentials during focal activation of multiple interneurons. Somatic whole-cell recordings have a modest impact on dendritic Cl⁻ homeostasis (Jarolimek et al., 1999; Khirug et al., 2005). Dialysis from the electrode solution would have served to reduce, not increase, the heterogeneity that we measured; we found no relationship between reversal potentials and distance from soma (see Fig. 7D). Patch pipettes with resistance of 5–7 MΩ were filled with an internal solution containing the following (in mM): 124 K-MeSO₄, 5 KCl, 10 KOH, 4 NaCl, 10 HEPES, 28.5 sucrose, 4 Na₂ATP, 0.4 Na₃GTP, and 1.4 mM MEQ, with osmolarity of 295 mOsm and pH 7.25–7.35. For visualizing the whole morphology of the recorded cells, 20 μM Alexa Fluor-594 hydrazide (Thermo Fisher Scientific) was added to the internal solution on the day of the experiment. Resting membrane potential (RMP) and input resistance were measured after whole-cell configuration was reached. Series resistance (R_s; assessed in voltage-clamp mode by –5 or –10 mV voltage step) was monitored for stability during the experiments. Only neurons with R_s < 20 MΩ were included in the analysis. For all the electrophysiological recordings, signal acquisition was performed using a Multiclamp amplifier (Multiclamp 700B, Molecular Devices) with Clampex 10 software (Molecular Devices). Signals were sampled at 10 kHz and filtered at 2 kHz. Data were stored on a PC for offline analysis after digitization using an analog-to-digital converter (Digidata 1440A, Molecular Devices).

RuBi-GABA uncaging

RuBi-GABA (purchased from Tocris Bioscience) stocks were prepared before the experiments and diluted in ACSF for a final concentration of 5 μM. The perfusate was protected from light during experiments to prevent RuBi-GABA photolysis before the recordings. Somatic or dendritic ROIs of pyramidal cells were chosen based on the sCLM expression, morphology of the cells, and no sign of injury or dendritic blebs. Two-photon sCLM images were acquired in XY scanning mode at 860 nm by a custom-designed software [LabVIEW (described above)] and with a 40×, 0.8 NA water-immersion objective (Olympus). The ROI for RuBi-

GABA uncaging was selected in targeted path scanning [TPS (theta pulse stimulation)] mode. The electrophysiology software triggered the laser and controlled the pulse duration. RuBi-GABA uncaging was performed at 750 nm. Laser intensity was increased until reliable GABA_A receptor-mediated currents were observed. E_{GABA} was measured as described above. Laser stimulation without the presence of RuBi-GABA did not induce currents.

Image analysis

To measure the stability of microdomains, colocalization analysis was performed by selecting an ROI and measuring YFP/CFP in each pixel of that ROI using a 2-dimensional spatial correlation subroutine of ImageJ (*x–y* coordinates subroutine) in which the *x* value represents the YFP/CFP ratio for a particular pixel in the first image, and the *y* value represents the YFP/CFP ratio for the same pixel in the second image (see Fig. 8B). The correlation between the two images was then calculated by the linear correlation for all pixels in the ROI (see Fig. 8D). Identical images, or images that had the YFP/CFP ratios for each pixel change by the same amount between the two images, would have a correlation coefficient of 1. This pixel-wise spatial correlation coefficient is reduced whenever the Cl⁻ concentration of a given pixel, as assessed by the YFP/CFP emission ratio, no longer matches the prior concentration. This could occur, for example, because of a change in the Cl⁻ concentration of a microdomain or the anatomic distribution of that microdomain. Pseudo-colored images of sCLM (Figs. 3, 4C,D) were generated by selecting the ROIs, measuring the YFP/CFP in each pixel of that ROI, and using the Pseudo-color Image Look-Up Tables Fiji subroutine. The pseudo-colored image of sCLM in Figure 4F was generated by reconstructing a flattened (2D) image using the Cl⁻-insensitive CFP intensity to weight the contribution of the YFP/CFP ratio of each pixel in a 3D image stack. Pseudo-color image of FLIM (see Fig. 7F) was generated by calibrating MEQ lifetime using the Stern–Volmer relationship and calculating [Cl⁻]_i (Fig. 4B; Verkman et al., 1989). FLIM experiments included the brighter membrane-impermeable dye Alexa Fluor-594 as well as MEQ in the recording pipette solution. The Alexa Fluor-594 (Cl⁻-insensitive) signal was used to define the intracellular pixels. [Cl⁻]_i was then calculated from the fluorescence lifetime of MEQ in those pixels. A 2D image was created from a 3D image stack by weighting the MEQ-derived [Cl⁻]_i values by the relative intensity of Alexa Fluor-594. The Alexa Fluor-594 signal intensity was used to determine the brightness of each pixel that was pseudo-colored based on the calculated [Cl⁻]_i. In pixels where MEQ signal was indistinguishable from background noise, no pseudo-color was assigned, and the pixel was colored using a grayscale Alexa Fluor-594 signal. The grayscale then demonstrated the dendritic structure in areas where the MEQ signal is inadequate. For noise analysis, a representative 30 min time series (180 frames) of acutely sliced CLM-expressing CA1 pyramidal cells imaged in the presence of TTX is compared with the noise acquired from a similar series acquired with the shutter closed (Fig. 4H). MATLAB is used to perform a line scan to represent each neuron as a vector of intensity values and to compute subsequent fast Fourier transforms (FFTs) of CLM YFP intensity and the corresponding channel closed-shutter noise intensity (see detailed noise analysis below). As the power spectra of more time-frame images are averaged, the power of noise from a closed shutter will converge to that of white noise. FFT power obtained from variations because of persistent structural differences such as microdomains will not converge to a white noise power spectrum, converging instead to a greater power difference from white noise than shutter noise (Fig. 4H).

Detailed noise analysis

To test whether the observed spatial variance in [Cl⁻]_i could arise from noise, we compared the averaged power spectra of the spatial frequencies of [Cl⁻]_i reporter CLM intensity values in the neurons to the power spectrum of closed-shutter noise. Noise analysis was performed with customized scripts and documentation code using MATLAB Fourier transform and image analysis functions. Of the two fluorescent components of CLM, Cl⁻-sensitive YFP was chosen and compared with the noise detected with the laser shutter closed over the same number of time frames for each neuron. Dendrites or soma were selected based on

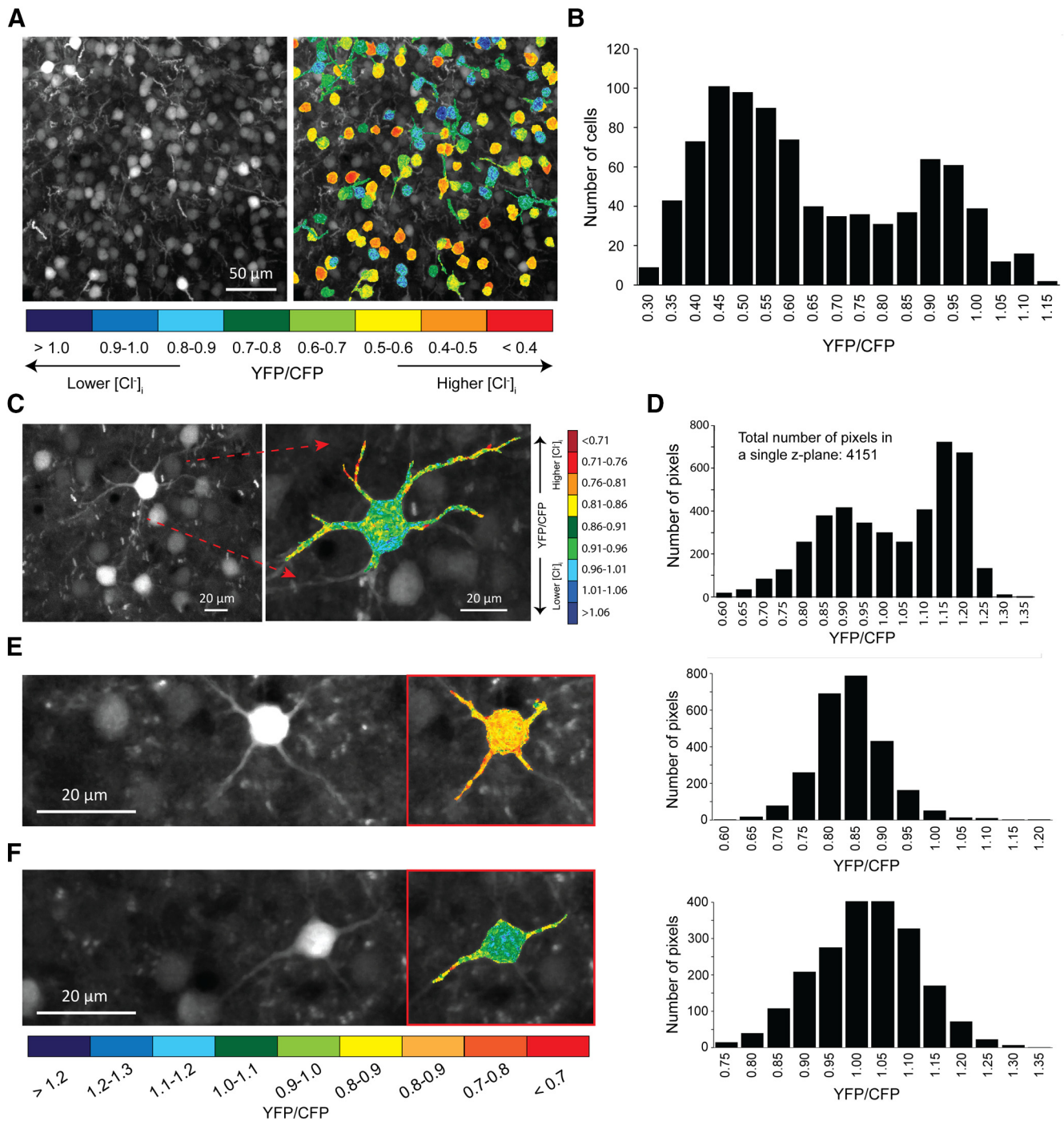


Figure 3. Evidence for the existence of chloride microdomains from *in vivo* sCLM imaging. **A**, Example of layer II/III cortical neurons expressing sCLM and their color-coded images in a P20 mouse. The data are presented as YFP/CFP ratios rather than $[Cl^-]$, because the calibration of sCLM is not feasible *in vivo* as a consequence of the limited capacity to permeabilize the membrane of target neurons and to manipulate the extracellular Cl^- concentration. **B**, A histogram of YFP/CFP ratios in hundreds of cells *in vivo*. **C–F**, Higher magnification of three sCLM-expressing cells and their color-coded images showing somatic and dendritic YFP/CFP values restricted to a single z-plane. The corresponding histograms demonstrate the range of YFP/CFP ratios in individual pixels.

persistent signal strength and linearized by line scan. The YFP signal of each frame was coregistered to the first frame and applied to both the YFP and closed-shutter noise image of that frame. Spatial FFTs were computed on these intensity signals to obtain the power (amplitude squared) of the observed YFP and closed-shutter noise values at a spectrum of wavelengths from 0.794 μm (exclusive) to 25.4 μm (inclusive), bound by the Nyquist wavelength and the distance equivalent to the largest exponent of base 2 that did not exceed the length of the smallest vector in pixels, respectively. The closed-shutter noise power spectra were rescaled by the ratio of the area under the curves between the mean

power spectrum of the neuronal signal and shutter noise. The white noise power spectrum was generated from averaging the power spectra of 72,000 vectors created from 400 random shuffles of each of 180 time frames. Defining $X_{1...180}$ as the vectors at 180 different time frames of observed intensity values for noise from a closed shutter or a signal from a neuron, we obtained 400 randomly shuffled versions for each 180 time-frame vectors $X_{1...180}$ assigned to $A_{1...72,000}$. By computing the FFT on each of the vectors $A_{1...72,000}$ and averaging the square of each result, we obtain the respective white noise power spectrum W for either a neuronal signal or closed-shutter noise defined as follows:

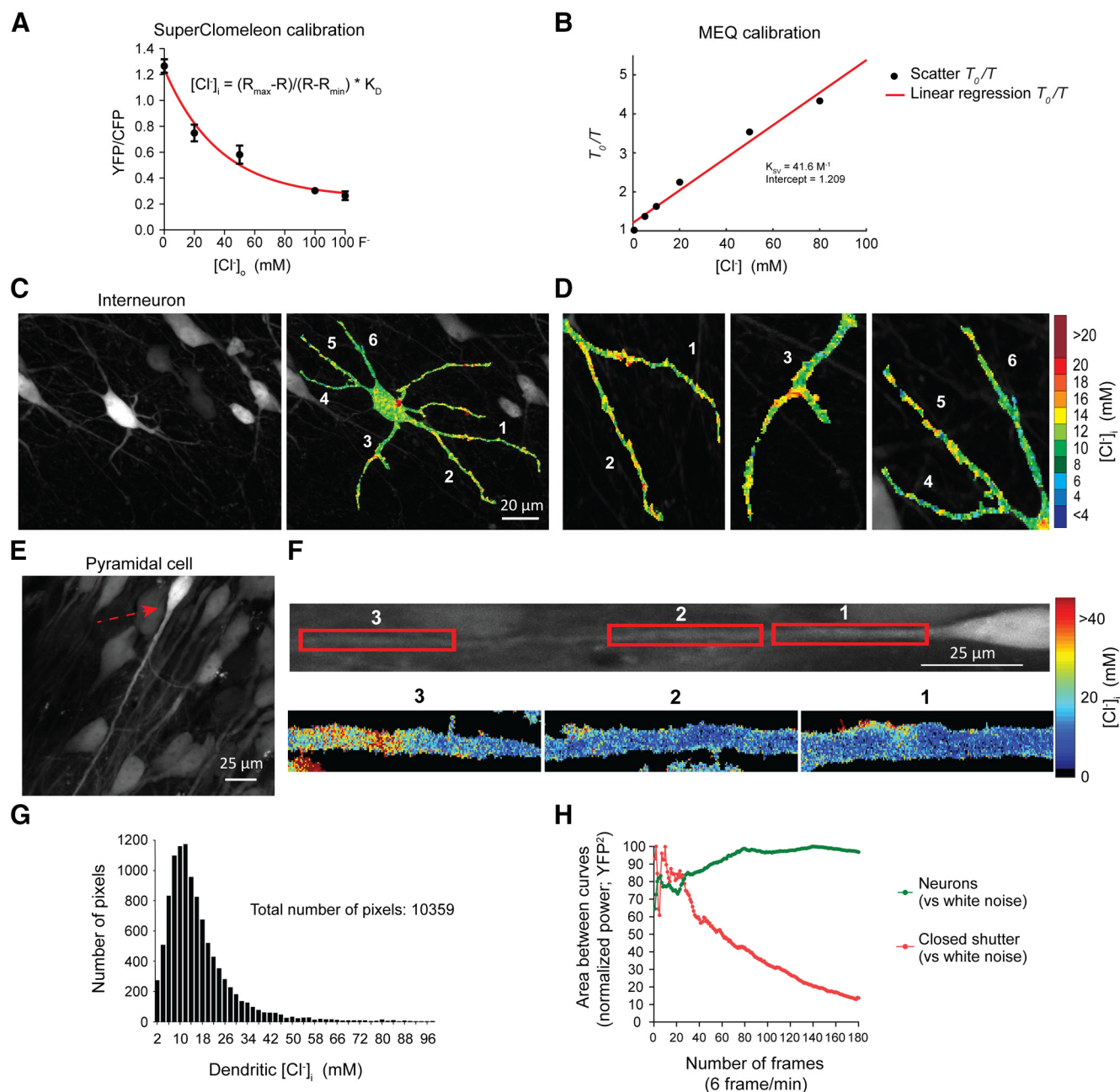


Figure 4. Evidence for the existence of chloride microdomains from *in vitro* sCLM imaging. **A**, sCLM was calibrated in organotypic slice cultures at different concentrations of Cl^- and in the presence of 50 μm of nigericin and 100 μm of tributyltin. With single-cell resolution, we calculated R_{max} , R_{min} , and K_d as described in Materials and Methods. Only neurons that responded to different Cl^- concentrations in extracellular media ($[\text{Cl}]_o$) were selected for final calculations. The range of values for R_{max} measured by two-photon microscopy in different calibration experiments was between 1.240 and 1.777. R_{min} ranged between 0.289 and 0.466. K_d was between 22.31 and 22.99 mM. For DualView imaging, R_{max} and R_{min} were 1.640 and 0.984 respectively. **B**, MEQ was calibrated using Stern–Volmer equation. MEQ was dissolved in the same solution as the internal pipette solution (K–MeSO₄-based) with different concentrations of Cl^- . **C**, **D**, Two-photon imaging of an organotypic slice culture showing a hippocampal interneuron (**C**) and the dendritic variations in $[\text{Cl}]_i$ (**D**). **E**, A CA1 pyramidal cell from a hippocampal organotypic slice-expressing sCLM. **F**, Top, The rotated neuron in **E** with a red arrow. Bottom, The magnified pseudocolored $[\text{Cl}]_i$ maps of different segments of the dendrite. **G**, Histogram of all pixels derived from the dendrite of the neuron depicted in **F**. **H**, CLM-expressing neurons were imaged for 30 min (180 frames at 6 frames/min). The deviation from a white noise power spectrum is plotted against the number of time frames for the mean power spectra of both the neuronal YFP signal and closed-shutter noise. The resulting normalized curves converge toward significantly different values and demonstrate a decreased time variance of the spatial distribution of the YFP signal versus normalized closed-shutter noise.

$$W = \text{mean}(\text{FFT}(A_1)^2, \text{FFT}(A_2)^2 \dots \text{FFT}(A_{72,000})^2)$$

The absolute area between the cumulative average of either the power spectra of the YFP neuronal signal or the closed-shutter noise and their respective white noise power spectrum was calculated at each time frame. The resulting curves were normalized and plotted as a function of frame number such that the number of frames included in the average power spectrum was equal to the frame number. Comparing the behavior of the averaged power spectra of signal intensity versus closed-shutter

noise as a function of the number of frame spectra averaged allowed a direct comparison of heterogeneity. The heterogeneity that is random and transient (i.e., noise) will average out with an increasing number of frames, but heterogeneity that is persistent will not.

Experimental design and statistical analysis

Imaging data were analyzed with ImageJ (<https://imagej.nih.gov/ij>) or MATLAB. Details of the analysis are included in the Image analysis section of Materials and Methods. Statistical analysis of the data was

performed in GraphPad Prism 8 (GraphPad Software). Statistics were assessed with two-tailed unpaired Student's *t* tests when comparing two groups. The number of data points (*n*) and the statistical significance (*p* value) are stated in the figure legends.

Results

Unique response of single pyramidal cells to individual inhibitory interneurons

We recorded single pyramidal cells using whole-cell patch clamping while selectively activating individual neighboring inhibitory interneurons in organotypic hippocampal slice preparations (Fig. 1A,B). We observed unique, reproducible values of E_{GABA} for each presynaptic interneuron recorded from a single pyramidal cell (Fig. 1C) whose distribution paralleled the broad range of previously reported E_{GABA} (Fig. 1D, Table 1). Our results demonstrate that individual interneurons have unique E_{GABA} values on postsynaptic pyramidal cells ($n = 40$ interneurons; $n = 10$ pyramidal cells; ~ 23 mV range in E_{GABA} ; Fig. 1E). The measured range may be an underestimate of the variance of synaptic E_{GABA} in these neurons because individual interneurons may have multiple synapses onto pyramidal cells (Somogyi et al., 1983; Buhl et al., 1994; Maccaferri et al., 2000; Bezair and Soltesz, 2013), each of which may have a different E_{GABA} value, and the somatic recording would reflect the combined currents from all synapses originating from the activated interneuron. Of note, not all stimulated interneurons evoked GABAergic currents in the recorded pyramidal cells; 56% of the stimulated interneurons resulted in recordable currents.

Evidence for dendritic chloride microdomains by fluorescence microscopy and electrophysiology

How can a single neuron express so many different values of E_{GABA} ? To investigate this, we measured the subcellular $[Cl^-]_i$ distribution in single neurons. To enable cell type-specific analysis of subcellular cytoplasmic Cl^- concentrations, we designed a conditional SuperClomeleon (*sCLM*) overexpression mouse line by generating a floxed stop/*sCLM* knockin at the *Rosa26* locus (Materials and Methods; Fig. 2). *sCLM* is a recently developed ratiometric Cl^- indicator with improved sensitivity compared with its predecessor CLM (Grimley et al., 2013). These fluorophores measure cytoplasmic Cl^- in many neurons and subcellular locations at once, without the perturbations of the intracellular milieu induced by whole-cell and perforated patch clamping. DNA Sanger sequencing confirmed the presence of the knocked-in *sCLM* allele (Materials and Methods; Fig. 2). Both heterozygous and homozygous mice were viable and fertile, and survived to adulthood without any abnormalities.

In vivo ratiometric two-photon fluorescence imaging was performed on anesthetized mice in which *sCLM* expression was driven by crosses with either *CamKII* or *Dlx* Cre mice to selectively express the fluorophore in principal cells or interneurons, respectively (see Materials and Methods). YFP/CFP values were compared in neurons of cortical layers II and III (Fig. 3A,B). We analyzed the dendrites located at the same imaging depth (Fig. 3C–F) to exclude the impact of depth-dependent differential scattering of cyan versus yellow light by the brain tissue (Boffi et al., 2018). The data are presented as YFP/CFP ratios rather than $[Cl^-]_i$ because the calibration of *sCLM* is not feasible *in vivo* (Arosio and Ratto, 2014; Boffi et al., 2018). This is a consequence of the limited capacity to permeabilize the membrane of target neurons and to manipulate the extracellular Cl^- concentration (Krapf et al., 1988). However, our data demonstrate a clear variance in YFP/CFP ratios in dendrites and soma (Fig. 3).

To analyze the subcellular Cl^- variance in a preparation in which *sCLM* YFP/CFP ratios can be quantitatively calibrated to $[Cl^-]_i$ (Fig. 4A), we performed two-photon high-resolution fluorescence microscopy of hippocampal organotypic slice cultures expressing *sCLM*. Our data demonstrate spatial variability of $[Cl^-]_i$ in the dendrites of individual neurons in the presence of 1 μM TTX (Fig. 4C–F). The individual pixels of the neuronal image depicted in Figure 4F demonstrate a wide range in dendritic $[Cl^-]_i$ (Fig. 4G). To examine the contribution of noise to these images, we performed time series imaging of *sCLM*-expressing neurons (180 images over 30 min). Fluorescence intensity arising from stable cytoplasmic $[Cl^-]_i$ microdomains would be expected to exhibit less temporal variance than noise. Over the 30 min observation period, the spatiotemporal variation in dendritic YFP intensity was much less than the corresponding variance of instrument noise (measured with the shutter closed and normalized to the YFP emission intensity; Figs. 4H, 5). This supports the presence of persistent spatial differences in $[Cl^-]_i$ that cannot be explained by noise. We estimated the size of the $[Cl^-]_i$ microdomains by analyzing the number of neighboring pixels (area, 0.09 μm^2) with similar $[Cl^-]_i$ (Fig. 6, single *z*-plane). Our data demonstrate that the size of microdomains varies between 1 and 10 pixels in a single neuron while the majority of microdomains were 1 pixel (Fig. 6F,G), suggesting that the dimensions of many microdomains were likely below the resolving power of two-photon microscopy.

To test whether the fluorescence measures of $[Cl^-]_i$ correlated with the electrophysiological assays of $[Cl^-]_i$, we conducted simultaneous measurements of the local dendritic $[Cl^-]_i$ using *sCLM* and $[Cl^-]_i$ calculated from E_{GABA} derived from gramicidin perforated patch-clamp recordings and local pressure application of 10 μM GABA in cultured hippocampal neurons (Fig. 7A). Local YFP/CFP ratios and $[Cl^-]_i$ measured by *sCLM* were highly correlated with the $[Cl^-]_i$ calculated by E_{GABA} (Fig. 7B,C). The correlation coefficient between the two measures was 0.65 ($n = 38$ ROIs; $n = 11$ cells; $p < 0.0001$; 95% confidence interval 0.41–0.80), consistent with the role of cytoplasmic microdomains in setting the local E_{GABA} (Delpire and Staley, 2014; Glykys et al., 2017). To estimate potential errors in the calculation of E_{GABA} because of inadequate dendritic space clamp (Staley and Mody, 1992), we tested for a correlation between the recorded E_{GABA} and the distance of the ROI from the center of soma. There was no significant correlation (Fig. 7D; $n = 38$ ROIs; $n = 11$ cells; $R = -0.20$, $p = 0.21$; 95% confidence interval, -0.49 to 0.12; Boffi et al., 2018).

sCLM retains the pH sensitivity of CLM (Grimley et al., 2013). Therefore, we therefore used a complimentary approach, assaying subcellular $[Cl^-]_i$ using the pH-insensitive, Cl^- -sensitive, single-wavelength fluorophore MEQ (Bowers and Verkman, 1991). We performed FLIM to avoid artifacts arising from subcellular variation in MEQ concentration. The FLIM measurements using MEQ delivered by the whole-cell recording pipette confirmed the variability of $[Cl^-]_i$ in dendrites of hippocampal pyramidal neurons in CA1 area (Figs. 4B, 7E,F). The variance in $[Cl^-]_i$ measured by MEQ FLIM was also highly correlated with simultaneous electrophysiological measurements of E_{GABA} measured in voltage-clamp neurons by local application of GABA using direct visual guidance ($n = 9$ ROIs; $n = 7$ cells; $R = 0.85$, $p = 0.003$; 95% confidence interval, -0.97 to -0.43 ; Fig. 7G). These data support the idea that subcellular variance in $[Cl^-]_i$ is a significant contributor to the variance in E_{GABA} (Table 1). We next measured the stability of E_{GABA} using two-photon RuBi-GABA uncaging (Fig. 7H). Rubi-GABA (Rial Verde et al., 2008) was photolyzed adjacent to the *sCLM*-expressing somatic or

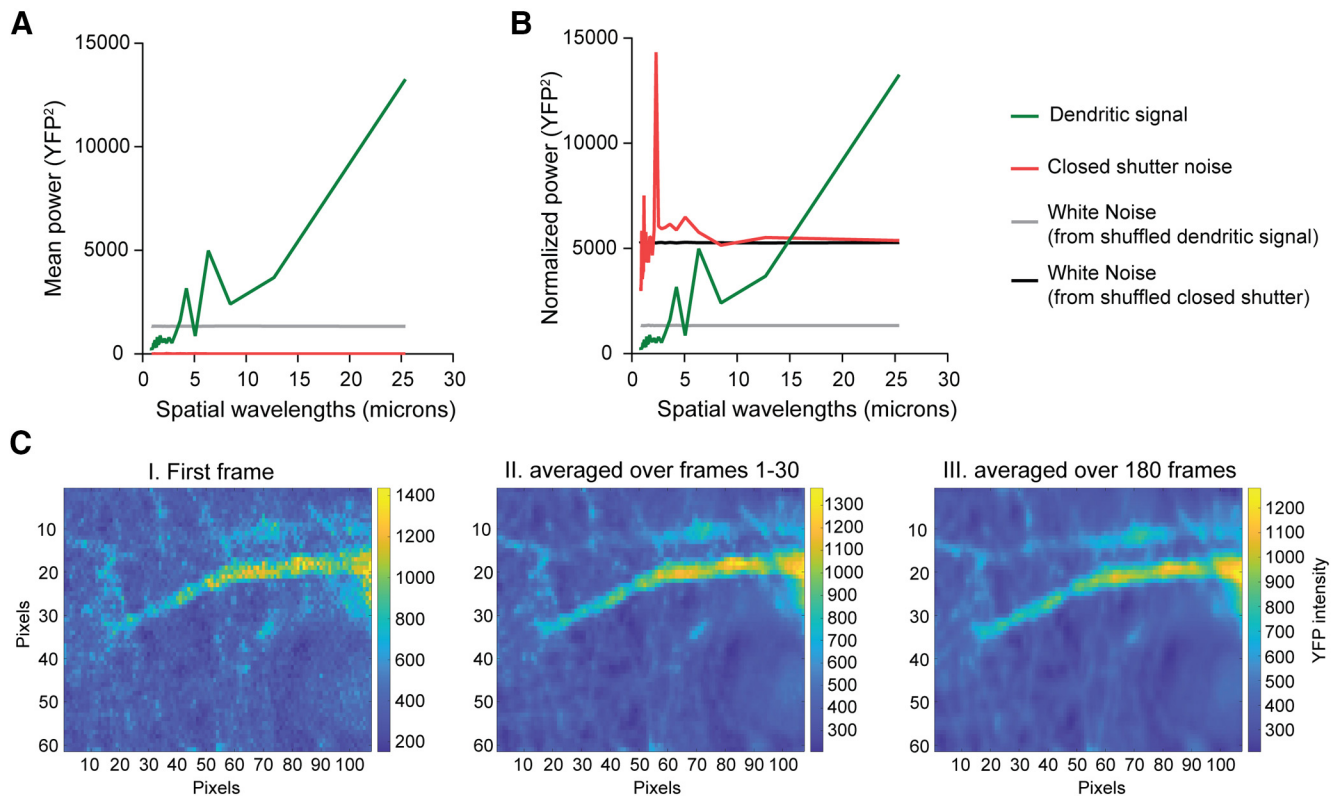


Figure 5. Signal versus noise analysis. **A**, From 180 CLM time frames, the absolute area between the mean power spectra and those of white noise for both the neuronal YFP fluorescence signal and closed-shutter noise is plotted against the number of time frames included in the mean (green and red, respectively). These are the raw curves, which are then normalized in **B**. **B**, The mean power spectrum of closed-shutter noise is normalized by a ratio to have total power equivalent to that of the mean power spectrum of the YFP dendritic signal (red and green, respectively). A white noise power spectrum is generated for either normalized shutter noise or dendritic signal (black and gray, respectively). **C**, YFP images that were used to generate the graphs in **A** and **B** show that while averaging decreases pixelation of the single frame (panel **I**), it does not change the dendritic map either after averaging the first 30 frames (panel **II**) or all 180 acquired frames (panel **III**). To decrease bleaching, these time-lapse images were acquired with lower laser power, which increases pixelation in a single frame compared with images in Figure 2.

dendritic ROIs. E_{GABA} was assessed by uncaging at intervals of 20 s at holding potentials from -120 to -10 mV. This assessment was repeated at the same ROI at an interval of 2–5 min to examine the activity dependence of the local E_{GABA} . There was no significant difference between the sequential E_{GABA} measurements at this level of receptor activation (Fig. 7I; pairs, $n = 8$; paired t test, $p = 0.36$).

Physiologic chloride microdomains are not defined by the activity of cation-chloride cotransporters

Changes in $[Cl^-]_i$ are readily observed in response to alterations of the equilibrium conditions for CCCs using either osmotic or ionic perturbations of the perfusate (Thompson et al., 1988; DeFazio et al., 2000; Dzhalala et al., 2010; Glykys et al., 2014a). This influence of transport equilibrium conditions on $[Cl^-]_i$ has led to the idea that CCCs can also set $[Cl^-]_i$ independently of the equilibrium conditions. To test the degree to which $[Cl^-]_i$ microdomains are defined by CCCs, we imaged sCLM in stable extracellular ionic and osmotic conditions. We acquired time-lapse images for 40–50 min (Fig. 8A). The ROIs (soma and dendrites of a single pyramidal neuron; Fig. 8B) were monitored and compared pixel by pixel with previous measurements every 10 min (Fig. 8C,D). Consistent with the prior noise analyses (Fig. 4H), the microdomains remained highly stable in control conditions. Applying a high concentration of furosemide to block NKCC1 and KCC2 simultaneously (Gillen et al., 1996) did not alter the microdomain distributions (Fig. 8D,E). Figure 8E shows the mean normalized Pearson's r by time [normalized to the initial

correlation coefficient and indicated as a percentage: at baseline in the absence of furosemide \pm SD: $97.81 \pm 8.43\%$, $n = 12$; after application of furosemide for 30 min \pm SD: $97.34 \pm 7.09\%$, $n = 12$; $p = 0.92$; effect size (d) = 1.42; 95% confidence interval, -10.82 to -9.86 ; $R^2 = 0.001$]. Because the mobility of Cl^- in neuronal cytoplasm is very high (Kuner and Augustine, 2000), $[Cl^-]_i$ should have rapidly homogenized after the blockade of CCCs if CCC activity had created the $[Cl^-]_i$ microdomains. The fact that this was not observed indicates that $[Cl^-]_i$ microdomains do not arise from local differences in cation- Cl^- transport rates. While the correlation coefficient was stable over 1 h, the value of the correlation coefficient was dependent on the expression levels of sCLM in different mice (Fig. 8F). This dependence supports the idea that the spatial variance in sCLM signal is distinct from noise. To assess the lower bound of spatial stability that could be resolved with this technique, the same region of interest was acquired with the microscope shutter closed to quantify the much lower correlation of noise between the images (Fig. 8B,D). As a positive control to demonstrate that millimolar changes in $[Cl^-]_i$ could be resolved with these techniques, somatic and dendritic $[Cl^-]_i$ were also measured in sCLM organotypic slices before and after seizure-like events (SLEs; Fig. 8G,H; Glykys et al., 2014a). Cultured hippocampal organotypic slices develop spontaneous epileptiform activities beginning late in the first day after slicing, which can be detected by chronic calcium imaging observation (Lillis et al., 2012; Jacob et al., 2019) and field potential electrophysiological recording (Dyhrfeld-Johnsen et al., 2010). Our data show that the returns to baseline in Figure 8, G and H, are monotonic (i.e., they do not jump between values of

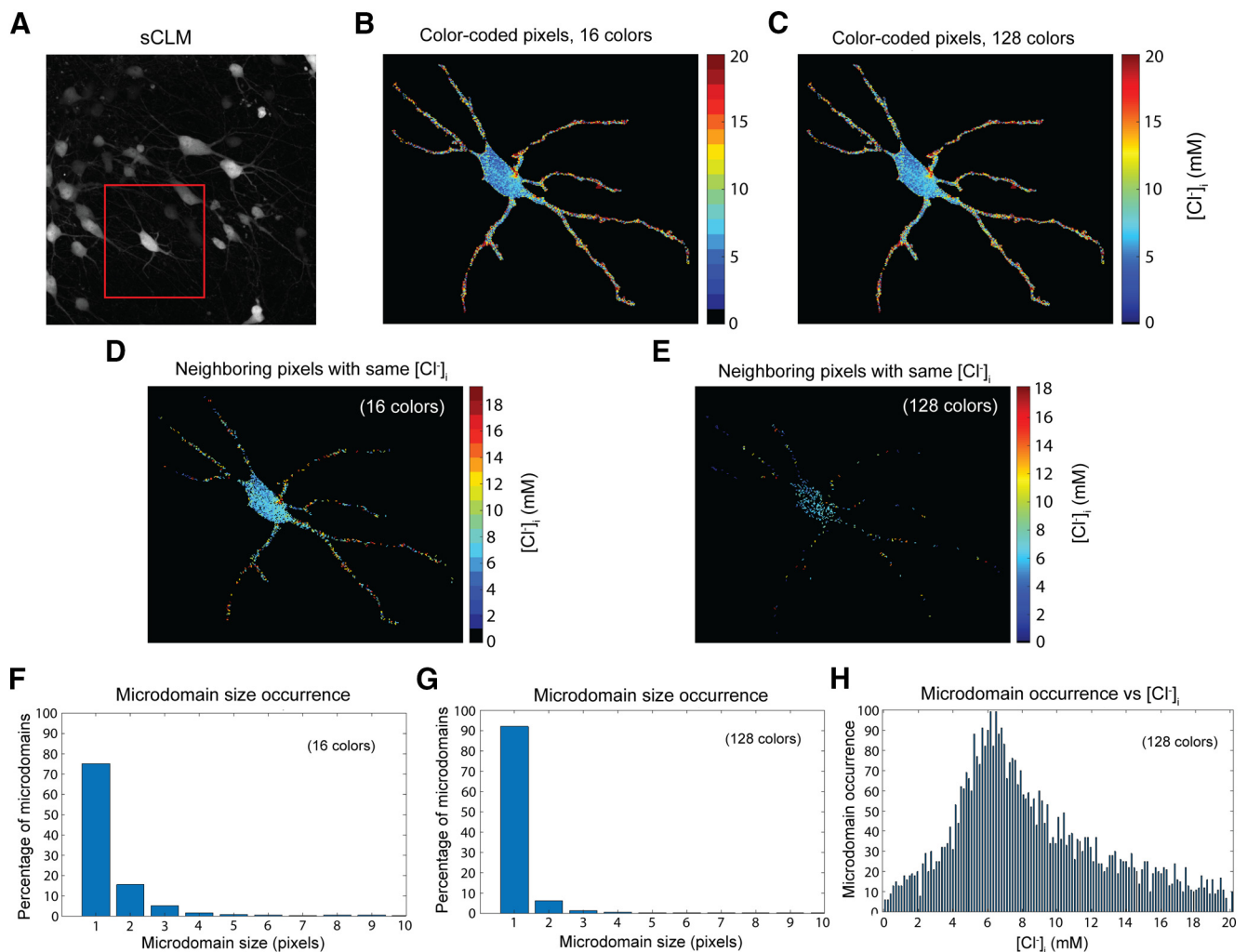


Figure 6. The size of $[Cl^-]_i$ microdomains. **A**, A sCLM-DLX-Cre organotypic slice shows sCLM-expressing interneurons. **B, C**, Pseudocolored images (labeled with 16 and 128 colors) of the neuron in the red box in **A** were generated to visualize the range of $[Cl^-]_i$ and estimate the size of $[Cl^-]_i$ microdomains. **D**, Microdomains defined as neighboring pixels (>1 pixel with the same color; i.e., $[Cl^-]_i$ values in the same bin) are shown in the 16-color image. **E**, Microdomains defined as in **D** based on the same data as in **A–D**, after binning into a 128-color pseudocolors. **F**, A histogram of the distribution of $[Cl^-]_i$ microdomain sizes derived from the 16-color image. **G**, A histogram of the distribution of $[Cl^-]_i$ microdomain sizes derived from the 128-color image. **H**, The number of $[Cl^-]_i$ microdomains in the 128-color image versus $[Cl^-]_i$.

$[Cl^-]_i$ that represent the smallest resolvable changes). Further, $[Cl^-]_i$ returns to baseline after SLEs, and the rate of return was independent of the initial (baseline) value. These results indicate that temporal fluctuations in $[Cl^-]_i$ can be resolved by this technique, and that $[Cl^-]_i$ microdomains persist after large transient Cl^- fluxes. As previously mentioned, sCLM is pH sensitive. However, changes in pyramidal cell cytoplasmic pH during seizures in hippocampal organotypic slices (Lillis et al., 2012) would lead to an underestimate of the ictal changes in $[Cl^-]_i$ measured with sCLM.

The stability of chloride microdomains is reduced by actin depolymerization

If the observed cytoplasmic Cl^- microdomains were created by the differential distribution of less mobile anionic macromolecules, then altering the distribution of those macromolecules should induce a corresponding change in Cl^- microdomains. Actin is one such macromolecule that could contribute to the structural basis for Cl^- microdomains. Actin is a variably branched cytoskeletal polyelectrolyte with a large negative surface charge (Castaneda et al., 2018) that is stationary once

polymerized into filamentous actin (F-actin; Watanabe and Mitchison, 2002). Actin is continuously polymerized and depolymerized, and the balance between these two processes can be altered by several well studied drugs (Fenteany and Zhu, 2003; Chia et al., 2016). One such drug is latrunculin B, which binds to actin monomers to inhibit actin assembly (Morton, 2000), thereby shifting the balance toward actin disassembly. Latrunculin B, 5 μM , has been demonstrated to preserve the dendritic structure of hippocampal pyramidal cells over a period of hours *in vitro* (Kim and Lisman, 1999). We first confirmed that this concentration of latrunculin B does not affect the shape of the dendrites by imaging CA1 pyramidal cells expressing the Cl^- -insensitive fluorophore TurboRFP (Fig. 9A). Following baseline imaging, RFP-expressing neurons were continuously imaged for an additional hour after being in the presence of 5 μM latrunculin B. Pixel-to-pixel (pixel-wise) correlation of dendritic and somatic ROIs from sequential images were compared with the baseline images (Fig. 9B). Our data confirm that the application of 5 μM latrunculin B did not change the shape of the neurons measured by pixelwise correlation of sequential images [initial normalized percentage change in Pearson's $r \pm SD$ (image 1 vs 2):

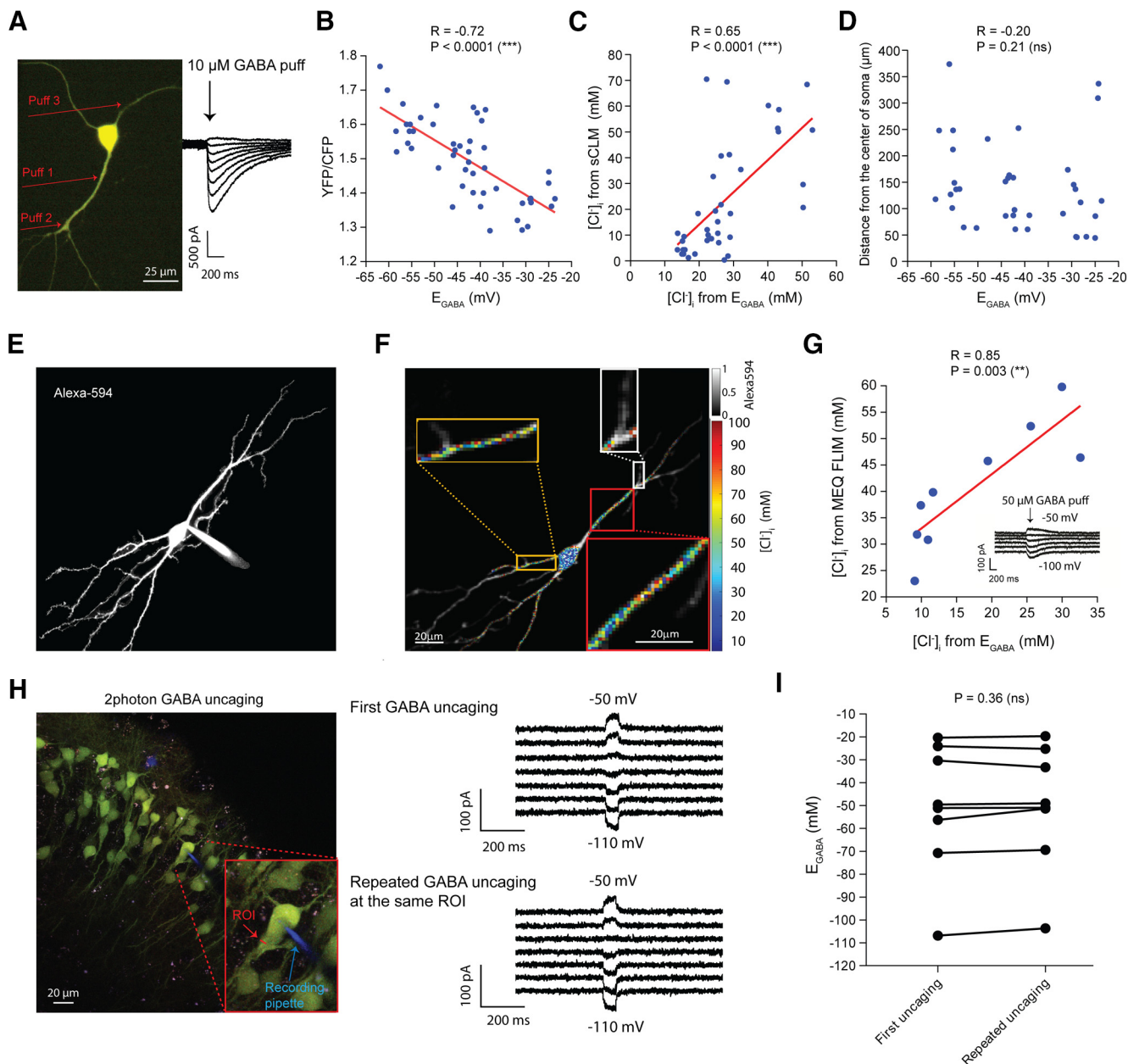


Figure 7. Simultaneous $[Cl^-]_i$ imaging and electrophysiology. **A**, A representative hippocampal-dissociated cultured neuron expressing sCLM and visualized by DualView using a CCD camera to simultaneously measure the YFP and CFP fluorescence. **B**, The $[Cl^-]_i$ measured by fluorophore data (YFP/CFP) and the $[Cl^-]_i$ calculated from E_{GABA} in dissociated cultured cells are highly correlated ($n = 38$ ROIs, 11 cells, $p < 0.0001$). **C**, There is a significant correlation between the $[Cl^-]_i$ measurements by sCLM and $[Cl^-]_i$ calculated by E_{GABA} ($n = 38$ ROIs, 11 cells, $p < 0.0001$). **D**, There was no significant correlation between the distance of selected ROIs from the center of soma and the recorded E_{GABA} ($n = 38$, 11 cells). **E**, A representative example of a hippocampal pyramidal cell loaded with Alexa Fluor-594 and Cl^- -sensitive, pH-insensitive dye, MEQ. **F**, Fluorescence lifetime imaging of $[Cl^-]_i$ in hippocampal neurons confirms the variance of $[Cl^-]_i$ in dendrites. $[Cl^-]_i$ calculated from MEQ lifetime is visualized in pseudocolor where the Alexa Fluor-594 ($[Cl^-]_i$ -insensitive) signal sets the transparency value such that the $[Cl^-]_i$ value and corresponding color relate solely to the MEQ lifetime while the brightness of the pixel is set by Alexa Fluor-594 as a structural marker (gray colorbar, top right). No averaging or clustering was performed on MEQ images. Note the variety of $[Cl^-]_i$ values and the frequent juxtaposition of relatively high and low values in close proximity. **G**, After loading the cells with MEQ, $50 \mu M$ GABA was puffed to different visualized segments of dendrites and E_{GABA} was measured. The $[Cl^-]_i$ measured by MEQ lifetime in that segment was compared with the $[Cl^-]_i$ calculated from the Nernst equation from the E_{GABA} measured electrophysiologically in the same segment. The two measures of $[Cl^-]_i$ are significantly correlated ($n = 9$ ROIs, 7 cells, $p = 0.003$). **H**, An example of a two-photon RuBi-GABA uncaging experiment on sCLM-expressing pyramidal cells. The red arrow shows the selected ROI, and the blue arrow points to the recording pipette containing Alexa Fluor-594. E_{GABA} was measured twice at the same ROI to examine the stability of the GABA-evoked currents. **I**, There was no significant difference between the first and second GABA uncaging-mediated E_{GABA} recordings (paired t test; pairs, $n = 8$; $p = 0.36$).

$-1.73 \pm 2.06\%$, $n = 11$; final normalized percentage change in Pearson's $r \pm$ SD after 1 h in $5 \mu M$ latrunculin B (image 1 vs 5): $-2.69 \pm 1.78\%$, $n = 11$, $p = 0.26$; Fig. 9B).

Next, we repeated the same experimental procedure in organotypic hippocampal slice cultures from sCLM transgenic mice (Fig. 9C). To exclude potential effects of cytoskeletal alterations on synapses and transporters, the experiments were performed

in the presence of $1 \mu M$ TTX, $10 \mu M$ bumetanide (NKCC1 blocker; Dzhalal et al., 2008), and $1 \mu M$ VU 0463271 (VU; a selective KCC2 blocker; Sivakumaran et al., 2015). Addition of $5 \mu M$ latrunculin B steadily changed the distribution of Cl^- microdomains, evidenced by a reduction in the pixel-wise correlation coefficient of sequential images (Fig. 9D) compared with the control conditions [i.e., the baseline images obtained in the

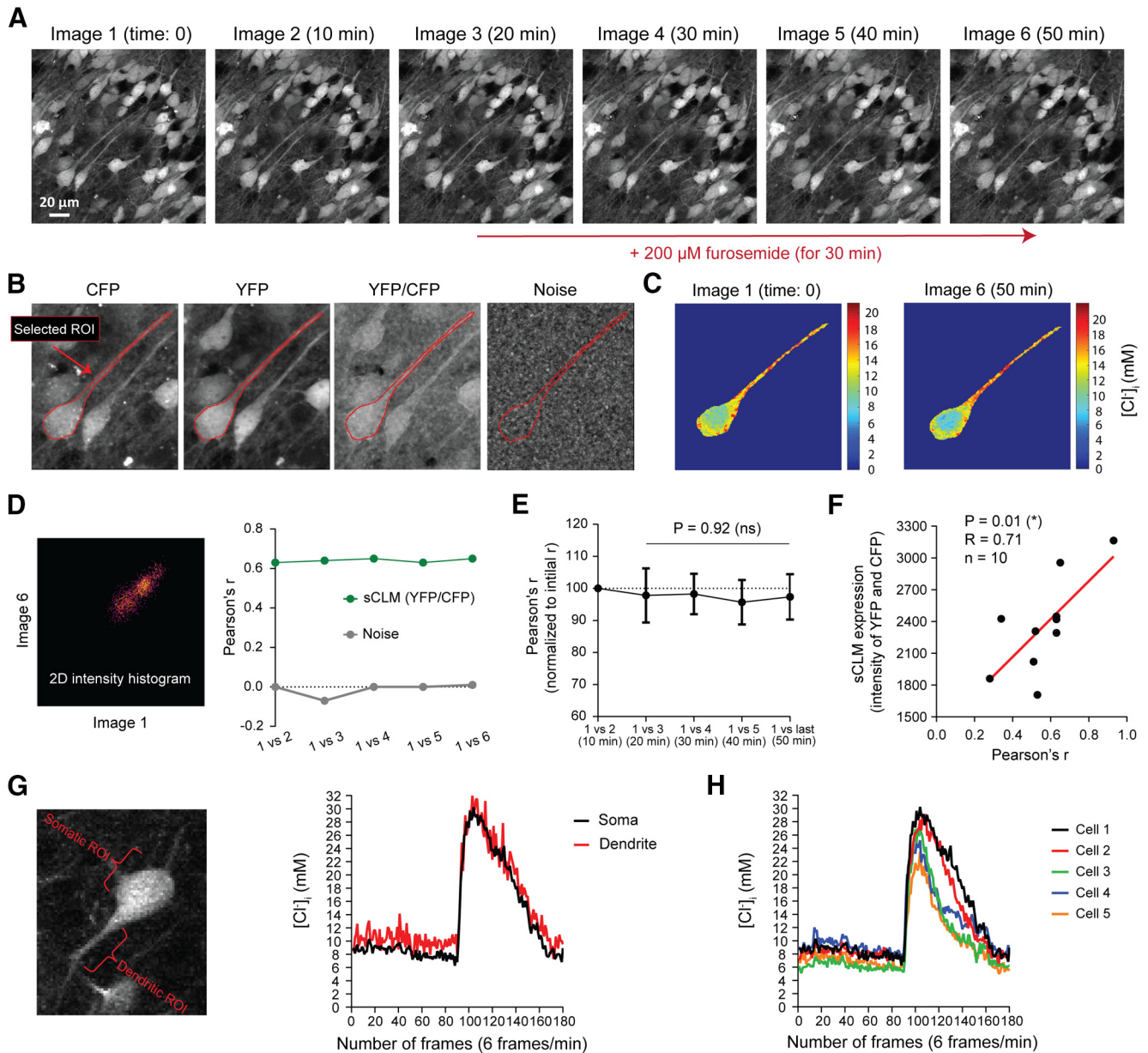


Figure 8. Chloride microdomains are stable and are not defined by Cl^- transport. **A**, Time-lapse images of a hippocampal pyramidal cell, expressing sCLM in the presence of $1 \mu\text{M}$ TTX before and after blocking KCC2 and NKCC1 with $200 \mu\text{M}$ furosemide. **B**, The stability of microdomains was measured by selecting an ROI and comparing YFP/CFP values in each pixel of that ROI over time. The same ROI was also imaged while the microscope shutter was closed to measure the noise level and pixel-by-pixel correlation of the ROI as a control. **C**, $[\text{Cl}^-]_i$ in soma and dendrite of the selected ROI before and after 30 min application of furosemide. **D**, Pixel intensity correlation analysis in time-lapsed images was performed by generating 2D intensity histograms and calculating Pearson's r , using the Fiji plugin Coloc2. The colocalization correlation analysis of the $[\text{Cl}^-]_i$ indicates that these dendritic Cl^- microdomains remain stable before and after the application of furosemide. **E**, The change in spatial correlation of the sequential ratiometric images (normalized to the maximum Pearson's correlation value obtained at baseline) demonstrates that the spatial stability of Cl^- microdomains does not change significantly over time after the application of $200 \mu\text{M}$ furosemide. **F**, The observed variability in Pearson's r in different experiments was significantly correlated with expression levels of sCLM. **G**, To demonstrate that small and large fluctuations in somatic and dendritic ROIs are detectable by sCLM imaging, sCLM-expressing cells were imaged before and after SLEs. **G** shows an example of a CA1 pyramidal neuron expressing sCLM, which was imaged for 30 min (6 frames/min; 180 total frames). Small changes in $[\text{Cl}^-]_i$ can be detected at baseline (preictal period), as well as a large Cl^- transient during an SLE in somatic and dendritic ROIs. **H**, Fluctuations in $[\text{Cl}^-]_i$ in five different somatic ROIs before and during an SLE.

presence of TTX, bumetanide, and VU alone; normalized mean percentage pixel-wise correlation coefficient by the end of imaging \pm SD for VU and bumetanide: $98.8 \pm 12.18\%$, $n = 15$; for latrunculin B: $77.3 \pm 10.54\%$, $n = 15$, $p = 0.002$, effect size (d) = 1.89; 95% confidence interval, -33.94 to -8.98 , $R^2 = 0.47$; Fig. 9D]. The mean percentage change in pixel-wise correlation coefficient in the presence of CCC antagonists (either high concentration of furosemide or bumetanide and VU: $-4.85 \pm 5.08\%$, $n = 23$ ROIs) was significantly less than the percentage change after the application of latrunculin B [$-24.0 \pm 9.84\%$; $p < 0.0001$; $n = 15$ ROIs; effect size (d) = 2.5; 95% confidence interval, -24.17 to

-14.32 ; $R^2 = 0.63$; Fig. 9E]. In addition to TurboRFP, the average pixel-wise correlation was also compared between CFP images as an extra control that did not significantly change during the same time period [transporter blockers, $-7.20 \pm 15.5\%$; latrunculin B, $-7.09 \pm 4.7\%$; $p = 0.98$; effect size (d) = 0.01; 95% confidence interval, -11.41 to 11.63 ; $R^2 = 2.95 \times 10^{-5}$]. The addition of latrunculin B to the perfusate containing transporter blockers did not alter the average percentage change of $[\text{Cl}^-]_i$ observed after transport block (transporter blockers: $14.76 \pm 18.13\%$, $n = 20$; latrunculin B: $14.74 \pm 14.07\%$, $n = 13$; $p = 0.90$; 95% confidence interval, -12.14 to 12.10 ; effect size = 0.001; $R^2 = 3.45 \times 10^{-5}$).

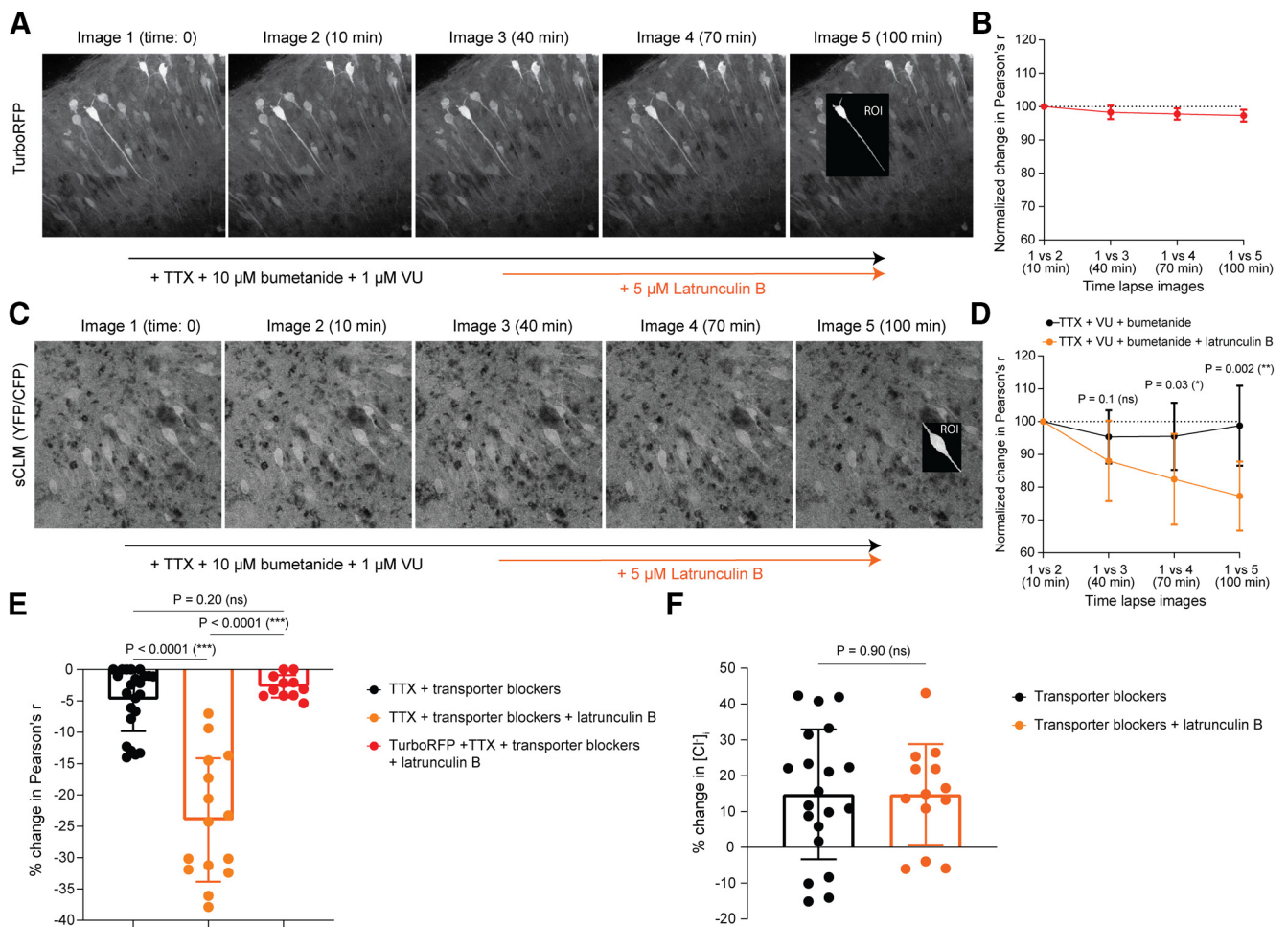


Figure 9. Contribution of cytoplasmic anionic immobile polymers to Cl^- microdomains. **A**, Time-lapse imaging of CA1 hippocampal cells expressing TurboRFP (a Cl^- -insensitive fluorophore) was performed in the presence of 1 μM TTX, 10 μM bumetanide, and 1 μM VU 0463271. Latrunculin B (5 μM) was added to the perfusate, and spatial correlation was performed before versus after drug-induced actin depolymerization. **B**, The pixel-by-pixel correlation of TurboRFP-expressing neurons were compared between images to measure the impact of latrunculin B on the morphology of neurons over an hour of drug application. **C**, Time-lapse imaging of CA1 hippocampal sCLM expressing cells was performed in the presence of 1 μM TTX, 10 μM bumetanide, and 1 μM VU 0463271. Latrunculin B was added to the perfusate and a pixel-by-pixel correlation was performed before versus after drug-induced actin depolymerization. **D**, The change in spatial correlation of the sequential ratiometric images (normalized to the maximum Pearson's correlation value obtained at baseline) demonstrates that the spatial stability of Cl^- microdomains decreases significantly over time after the addition of 5 μM latrunculin B. **E**, Comparing the average pixelwise spatial correlation coefficient in all experiments shows that the correlation significantly decreased after the addition of latrunculin B compared with transporter block alone (either high concentration of furosemide or bumetanide and VU). The average pixelwise correlation is also shown for TurboRFP images as control. **F**, $[Cl^-]_i$ averaged over the entire ROIs is not changed by the addition of latrunculin B to the perfusate. Data are presented as the mean \pm SD.

007; Fig. 9F). These findings indicate that although CCCs are actively transporting Cl^- across the membrane in this preparation, the CCCs do not define the distribution of microdomains. In contrast, latrunculin B modified $[Cl^-]_i$ microdomains without changing the average $[Cl^-]_i$ by altering the macromolecular distribution through anionic biopolymer disassembly.

Discussion

These data obtained using multiple complimentary recording techniques support the existence of stable $[Cl^-]_i$ microdomains that underlie unique responses to local GABA_A receptor activation in the dendritic cytoplasm of hippocampal neurons. Our studies extend the variance of E_{GABA} and $[Cl^-]_i$ between neurons (Table 1; Glykys et al., 2014a,b; Sato et al., 2017) to focus for the first time on the subcellular variation of Cl^- in individual dendrites. The stability of microdomains over the entire time interval for which stability could be assessed, and the wide variance in the E_{GABA} of pyramidal cells measured when individual presynaptic interneurons were stimulated, underscore the potential

functional importance of $[Cl^-]_i$ microdomains for signaling at GABAergic synapses.

The sizes of Cl^- microdomains varied both in concentration and anatomic extent (Fig. 6), and many microdomains are likely below the resolution of two-photon microscopy, as would be expected based on the proposed mechanism of Cl^- distribution (Fig. 10). Pixel-wise histograms of Cl^- distribution varied from one dendrite to the next (Fig. 3, compare D, E, F; compare Fig. 3D–E, 4G), so there is not a single mean and variance of $[Cl^-]_i$ microdomains.

Neuronal Cl^- microdomains have been a source of confusion and controversy. A wide variety of experimental evidence supporting the nonuniform distribution of cytoplasmic Cl^- (Barna et al., 2001; Duebel et al., 2006; Szabadics et al., 2006; Földy et al., 2010; Glykys et al., 2014a; Berglund et al., 2016; Untiet et al., 2016; Zorrilla de San Martin et al., 2017) has been challenged primarily by theoretical arguments (Luhmann et al., 2014; Doyon et al., 2016; Savtchenko et al., 2017; Düsterwald et al., 2018). The simplest argument for the existence of neuronal cytoplasmic Cl^- microdomains is the fact that the vast majority of anions in the

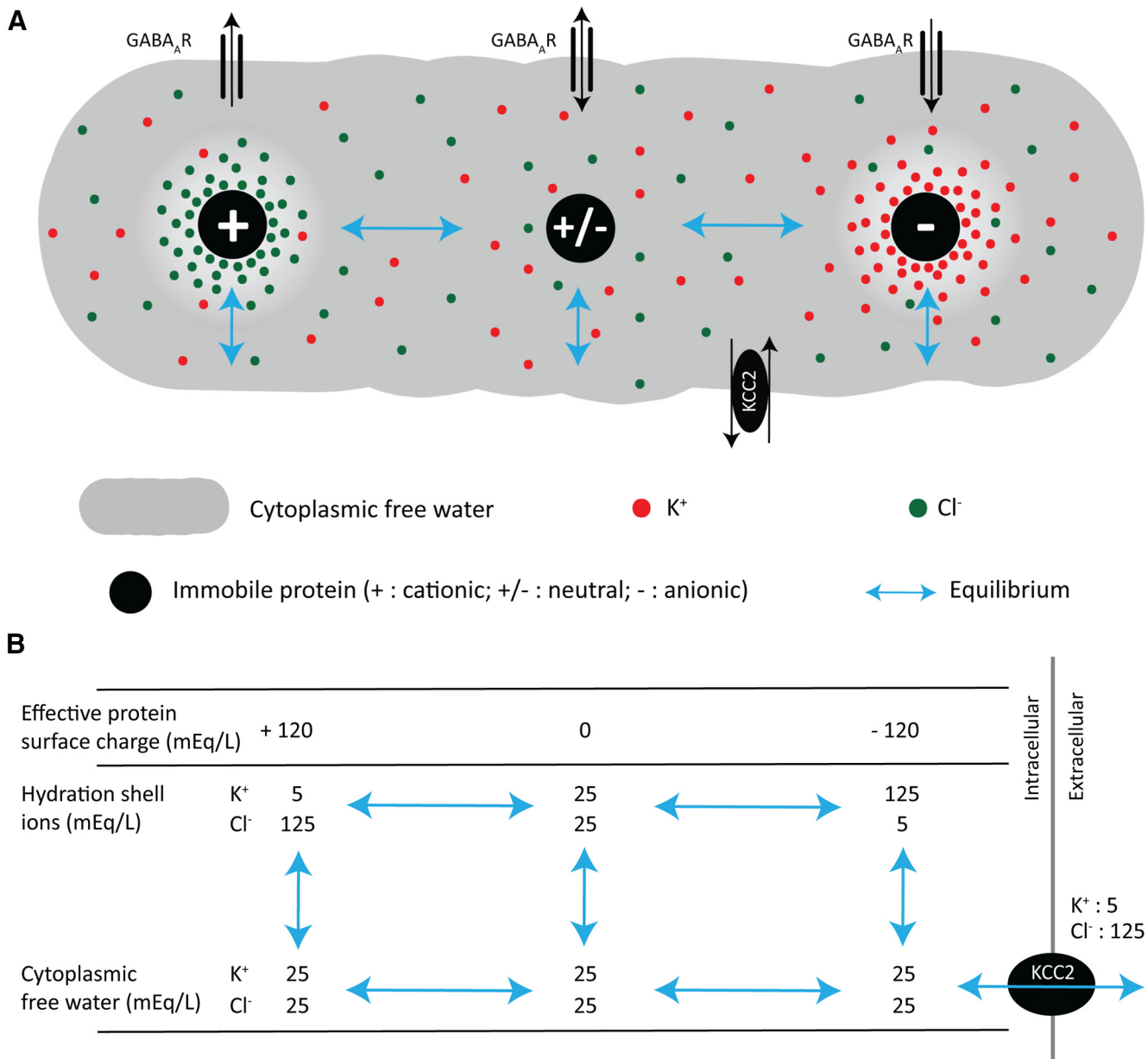


Figure 10. Stoichiometric membrane chloride cotransporters can be at equilibrium over the range of cytoplasmic chloride concentrations observed in this study. **A**, Effects of nonuniform distribution of immobile charges on the distributions of mobile cationic and anionic ions and GABA_AR ion flow. All mobile ions in the illustrated regions of the protein hydration shell are in equilibrium with the mobile ions in the cytoplasmic free water. The Donnan criteria (local charge balance and equal free energies across equilibria) are fulfilled between each region of the protein hydration shell and the free water, and between all regions of the free water. There is no net ionic diffusion between the cytoplasmic free water and the hydration shells because of the effects of fixed protein surface charges. Most cytoplasmic proteins bear a substantial net negative surface charge, which attracts cations and repels anions. Thus, most cytoplasmic K⁺ resides in the hydration shells of anionic proteins, and most Cl⁻ resides in the cytoplasmic free water. Consequently, the mean cytoplasmic K⁺ concentration is greater than the K⁺ concentration in the cytoplasmic free water, and the mean cytoplasmic Cl⁻ is less than the Cl⁻ in the free water. KCC2 is shown in equilibrium with the ions in the cytoplasmic free water. The higher ion concentrations in hydration shells near the high fixed surface charge density of the charged proteins do not drive additional water movement (Helfferich, 1995, chapter 5). **B**, The concentrations shown in **B** are an example to demonstrate the ionic equilibrium of KCC2 over the ranges of chloride observed in the current study. The example is for illustration only; we do not know the actual ionic activities in the protein hydration shells or cytoplasmic free water. The example values for spatially varying [Cl⁻]_i and [K⁺]_i demonstrate that local E_{GABA} could vary from 0 to -82 mV while maintaining equilibrium with KCC2-mediated KCl membrane transport.

cytoplasm are relatively immobile. In neurons, the GABA_A-permeant ions Cl⁻ and HCO₃⁻ together make up only a minority of the intracellular anions. The rest of the intracellular anions are amino acids and phosphates (Morawski et al., 2015), of which only a small minority are not associated with macromolecules (Masuda et al., 1990; Veech et al., 2002), such as nucleic acid species (Manning, 1978) and proteins (Gianazza and Righetti, 1980). These immobile anionic polymers are not uniformly distributed in the cytoplasm (Gut et al., 2018; Chen et al., 2020), so

it is reasonable to expect that there is a nonuniform distribution of mobile anions to compensate for the distribution of immobile anions. Macroscopic nonuniform distributions of mobile ions are readily demonstrated experimentally using gels with fixed anionic charges (Procter, 1914; Fatin-Rouge et al., 2003; Golmohamadi et al., 2012), and these findings extend to anionic biopolymers that are not crosslinked into gels (Marinsky, 1985). Here we demonstrate that the inhibition of polymerization of one such anionic macromolecule, actin, led to a proportionate

change in the distribution of Cl^- microdomains (Fig. 9). The distribution of the mobile anion Cl^- reflects the net combined effect of the spatial distribution of multiple immobile ions. The term “microdomains” may obscure the fact that the dimensions of the inhomogeneous distribution of mobile anions in the cytoplasm should extend down to the Debye layers of the atomic constituents of these immobile charged polymers (Fig. 6).

The concentration-independent assays of the fluorophores sCLM and MEQ enabled spatial averaging of the chloride concentrations within the minimum resolvable area of these techniques [i.e., 1 pixel ($0.156 \mu\text{m}^2$)]. The fact that $[\text{Cl}^-]_i$ differences persist over time demonstrates that the interpixel $[\text{Cl}^-]_i$ values reflect displacement by time-invariant charged cytoskeletal structural elements (Fig. 8A–E). Similarly, the observed changes in $[\text{Cl}^-]_i$ during seizure activity with subsequent return to baseline (Fig. 8G,H) support a time-invariant, structural basis for $[\text{Cl}^-]_i$ microdomains arising from stable local immobile anion concentrations. Additional support for this model comes from the finding that disruption of one such immobile anion, F-actin, causes a concurrent disruption of $[\text{Cl}^-]_i$ without disrupting cell morphology (Fig. 9).

Cl^- is not the only cytoplasmic ion whose spatial distribution would be affected by immobile anionic polymers. Because of electrostatic interactions, the concentration of cations is much higher in the hydration shells of these anionic polymers than in the free water that surrounds the shell (Gregor, 1951; Marinsky, 1993). This cytoplasmic inhomogeneity in cation concentration may provide insight into a long-standing problem: how can the high-velocity, membrane CCCs be at equilibrium over the wide range of observed steady-state values of $[\text{Cl}^-]_i$ (Table 1)? The simple ionic stoichiometry of the transporters (Voipio and Kaila, 2000), coupled with their high transport velocity (Thompson et al., 1988; Staley and Proctor, 1999; Jin et al., 2005; Alfonsa et al., 2015) and presumed homogeneous cytoplasmic cation concentrations should lead to homogeneous $[\text{Cl}^-]_i$, but this is not observed (e.g., Figs. 3, 4, Table 1). However, if the local cytoplasmic cation concentration also varies, then a much wider range of local steady-state $[\text{Cl}^-]_i$ could be in equilibrium with the CCCs resulting in cytoplasmic Cl^- microdomains (Fig. 10).

The local variance of the concentrations (or more accurately, the activities) of local cations and anions provides a means to reconcile the findings of transport biology (Voipio and Kaila, 2000; Doyon et al., 2016) with the impact of Donnan effects (Glykys et al., 2014a). That is to say, if transport is at equilibrium in each microdomain, then the highly regulated expression, phosphorylation, and membrane trafficking of these transporters (Stein et al., 2004; Lee et al., 2010; Heubl et al., 2017; Garand et al., 2019) may serve to tailor transport to the characteristics of each microdomain, maintaining volume and average Cl^- flux.

A related question is: if impermeant anions rather than transporters set E_{GABA} , why does the inhibition of specific cotransporters cause small fractional changes in measured $[\text{Cl}^-]_i$ (Fig. 9F) or E_{GABA} (Hübner et al., 2001; Dzhalala et al., 2005; Sipilä et al., 2009; Goutierre et al., 2019)? First, after CCC blockade or knockdown, E_{GABA} does not shift to RMP (Hübner et al., 2001; Brumback and Staley, 2008; Rinke et al., 2010; Goutierre et al., 2019) and $[\text{Cl}^-]_i$ does not shift to a passive distribution (Glykys et al., 2014a; Sato et al., 2017), as would be predicted if transporters set E_{GABA} . Second, neuronal membrane permeability to Cl^- is composed of multiple Cl^- cotransporters, channels and exchangers in addition to KCC2 and NKCC1. In the system described by Donnan (1911), the membrane cationic and anionic permeabilities are independent of each other. In neurons, for each

membrane Cl^- cotransporter, the Cl^- permeability is linked to the transport of another molecular species with its own transmembrane free energy gradient. The sum of the activities of the different cotransporters, channels, and exchangers approximates an independent Cl^- permeability (Glykys et al., 2014a, 2017). However, pharmacological block of any one element of this composite membrane Cl^- permeability will shift the equilibrium $[\text{Cl}^-]_i$ accordingly. Fluorescence imaging of large numbers of neurons demonstrate that these shifts occur in both directions after the inhibition of each CCC (Glykys et al., 2014a; Sato et al., 2017), as would be expected if neurons have unique transmembrane ionic gradients and local compliments of Cl^- transporters. The inhibition of both major CCCs at the same time led to very modest effects on $[\text{Cl}^-]_i$ microdomains (Figs. 8C,E, 9D,E), consistent with prior findings (Glykys et al., 2014a; Sato et al., 2017). In contrast, alteration of the distribution of anionic cytoskeletal polymers by the inhibition of actin polymerization induced corresponding shifts in cytoplasmic Cl^- microdomains (Fig. 9D,E).

The heterogeneity of $[\text{Cl}^-]_i$ provides a potential explanation for the higher $[\text{Cl}^-]_i$ reported by fluorophores versus the $[\text{Cl}^-]_i$ recorded by electrophysiological measurements (Glykys et al., 2009; Dzhalala et al., 2012; Sato et al., 2017; Table 1). For example, a fluorophore sensing the Cl^- in cytoplasmic free water but not the Cl^- in the hydration shells of anionic macromolecules will return a value higher than the mean cytoplasmic Cl^- . And if the fluorophore aligns with cationic regions of immobile proteins, it could report $[\text{Cl}^-]_i$ in those local hydration shells that are substantially higher than the mean cytoplasmic Cl^- (Fig. 10). These effects may also contribute to the wide range of $[\text{Cl}^-]_i$ in small neighboring microdomains (Fig. 6).

Other proposed explanations for the heterogeneity of neuronal $[\text{Cl}^-]_i$ include variation in the stoichiometry of Cl^- cotransport (Brumback and Staley, 2008), obligatory water cotransport (Delpire and Staley, 2014; Glykys et al., 2019), and a low V_{max} (maximum velocity) of transport relative to membrane Cl^- flux (Doyon et al., 2016; Düsterwald et al., 2018). The last of these explanations appears to be a special case, because E_{GABA} at any synapse would be quite unstable within the physiological range of synaptic activity due to temporal fluctuations in synaptic Cl^- influx versus saturable cotransport operating at V_{max} . Such temporal instability has only been observed at the maximal attainable levels of synaptic activity (Fig. 8G,H; Huguenard and Alger, 1986; Staley et al., 1995; Köhling et al., 2000; Krishnan and Bazhenov, 2011; Alfonsa et al., 2015; Silayeva et al., 2015; Buchin et al., 2016; Khazipov, 2016; Raimondo et al., 2017; Burman et al., 2019). The data presented here are most consistent with the idea that the equilibrium value of $[\text{Cl}^-]_i$ is defined by the local distribution of cytoplasmic anionic biopolymers. CCCs maintain that equilibrium value in the face of anionic membrane currents. This role for active Cl^- cotransport becomes critical as the rate of synaptic activity increases (Staley and Proctor, 1999; Glykys et al., 2009, 2014a; Doyon et al., 2016), for example, during seizure activity (Dzhalala and Staley, 2020). The proposal that the observed Cl^- distribution by displacement is relevant only at low rates of synaptic activity *in vitro* (Doyon et al., 2016; Düsterwald et al., 2018) is not consistent with *in vivo* measurements (Fig. 3). The low rates of synaptic activity *in vitro* and in the presence of TTX should dramatically reduce the discrepancy between measured E_{GABA} and the equilibrium conditions for cation– Cl^- cotransport if active transport were the primary mechanism of setting E_{GABA} . This would homogenize E_{GABA} at the potassium reversal potential for neurons expressing the KCl cotransporter KCC2, but this effect has not been observed (Figs. 3, 4, Table 1; Glykys et al., 2014a; Sato et al., 2017).

The range of variance of E_{GABA} determined by the activation of local interneurons agrees well with the ranges observed using perforated patch techniques (Fig. 1, Table 1). These values are a subset of the potential range of $[Cl^-]_i$ (Fig. 10). This subset of $[Cl^-]_i$ values raises the possibility of actively maintained motifs of immobile anions near the intracellular and extracellular faces of the channels opened by GABA_A receptors. The range of E_{GABA} could be actively maintained by the local density and post-translational modifications of anionic intracellular structural species, such as gephyrin, actin, and tubulin (Sola et al., 2001), and extracellular sulfated glycosaminoglycans (Glykys et al., 2014a,b, 2017).

The wide range of intraneuronal E_{GABA} directly impacts the direction and magnitude of the response to GABA released from each interneuron, and potentially at each GABAergic synapse. This increases the range of possible interactions between GABAergic and excitatory inputs to include not only hyperpolarizing and shunting inhibition but also synapse-specific amplification of excitatory inputs (Gulledge and Stuart, 2003; Grienberger et al., 2017). The observed 25 mV range in E_{GABA} is continuously distributed. This distribution is not consistent with a result arising from inadvertent stimulation of two interneuron subtypes with distinct E_{GABA} (Szabadics et al., 2006; Földy et al., 2010; Armstrong and Soltesz, 2012). Our findings do not invalidate those studies regarding E_{GABA} versus interneuron subtypes. Rather, the subtype of presynaptic interneuron may be one of several important variables that determine E_{GABA} at each pyramidal cell GABA_A synapse.

We have proposed new ideas for the mechanism of cytoplasmic Cl^- regulation and the heterogeneity in intracellular Cl^- of individual dendrites. These findings provide the first steps for future studies on the impact of anionic macromolecules such as actin in determining the neuronal Cl^- microdomains. In addition, future studies to elucidate the cellular and synaptic specificity of the polarity of GABA signaling, the time range over which this polarity is stable, and its plasticity will clarify the role of neuronal cytoplasmic Cl^- domains in neuronal signal processing and pathologic states, such as medically intractable epilepsy (Cohen et al., 2002; Spruston et al., 2016).

References

- Alfonsa H, Merricks EM, Codadu NK, Cunningham MO, Deisseroth K, Racca C, Trevelyan AJ (2015) The contribution of raised intraneuronal chloride to epileptic network activity. *J Neurosci* 35:7715–7726.
- Armstrong C, Soltesz I (2012) Basket cell dichotomy in microcircuit function. *J Physiol* 590:683–694.
- Arosio D, Ratto GM (2014) Twenty years of fluorescence imaging of intracellular chloride. *Front Cell Neurosci* 8:258.
- Astorga G, Bao J, Marty A, Augustine GJ, Franconville R, Jalil A, Bradley J, Llano I (2015) An excitatory GABA loop operating *in vivo*. *Front Cell Neurosci* 9:275.
- Balena T, Acton BA, Woodin MA (2010) GABAergic synaptic transmission regulates calcium influx during spike-timing dependent plasticity. *Front Synaptic Neurosci* 2:16.
- Barmashenko G, Hefft S, Aertsen A, Kirschstein T, Köhling R (2011) Positive shifts of the GABA_A receptor reversal potential due to altered chloride homeostasis is widespread after status epilepticus. *Epilepsia* 52:1570–1578.
- Barna B, Kuhnt U, Siklós L (2001) Chloride distribution in the CA1 region of newborn and adult hippocampus by light microscopic histochemistry. *Histochem Cell Biol* 115:105–116.
- Beaudoin GM III, Lee S-H, Singh D, Yuan Y, Ng Y-G, Reichardt LF, Arikath J (2012) Culturing pyramidal neurons from the early postnatal mouse hippocampus and cortex. *Nat Protoc* 7:1741–1754.
- Berglund K, Schleich W, Krieger P, Loo LS, Wang D, Cant NB, Feng G, Augustine GJ, Kuner T (2006) Imaging synaptic inhibition in transgenic mice expressing the chloride indicator, Clomeleon. *Brain Cell Biol* 35:207–228.
- Berglund K, Wen L, Dunbar RL, Feng G, Augustine GJ (2016) Optogenetic visualization of presynaptic tonic inhibition of cerebellar parallel fibers. *J Neurosci* 36:5709–5723.
- Bezaire MJ, Soltesz I (2013) Quantitative assessment of CA1 local circuits: knowledge base for interneuron-pyramidal cell connectivity. *Hippocampus* 23:751–785.
- Biwersi J, Verkman AS (1991) Cell-permeable fluorescent indicator for cytosolic chloride. *Biochemistry* 30:7879–7883.
- Biwersi J, Farah N, Wang Y-X, Ketcham R, Verkman A (1992) Synthesis of cell-impermeable Cl⁻-sensitive fluorescent indicators with improved sensitivity and optical properties. *Am J Physiol Cell Physiol* 262:C243–C250.
- Boffi JC, Knabbe J, Kaiser M, Kuner T (2018) KCC2-dependent steady-state intracellular chloride concentration and pH in cortical layer 2/3 neurons of anesthetized and awake mice. *Front Cell Neurosci* 12:7.
- Brumback AC, Staley KJ (2008) Thermodynamic regulation of NKCC1-mediated Cl⁻ cotransport underlies plasticity of GABA_A signaling in neonatal neurons. *J Neurosci* 28:1301–1312.
- Buchin A, Chizhov A, Huberfeld G, Miles R, Gutkin BS (2016) Reduced efficacy of the KCC2 cotransporter promotes epileptic oscillations in a subiculum network model. *J Neurosci* 36:11619–11633.
- Buhl EH, Halasy K, Somogyi P (1994) Diverse sources of hippocampal unitary inhibitory postsynaptic potentials and the number of synaptic release sites. *Nature* 368:823–828.
- Burman RJ, Selve JS, Lee JH, van den Berg M, Calin A, Codadu NK, Wright R, Newey SE, Parrish RR, Katz AA, Wilmshurst JM, Akerman CJ, Trevelyan AJ, Raimondo JV (2019) Excitatory GABAergic signalling is associated with acquired benzodiazepine resistance in status epilepticus. *Brain* 142:3482–3501.
- Castaneda N, Zheng T, Rivera-Jacquez HJ, Lee H-J, Hyun J, Balaff A, Huo Q, Kang H (2018) Cations modulate actin bundle mechanics, assembly dynamics, and structure. *J Phys Chem B* 122:3826–3835.
- Chia JX, Efimova N, Svitkina TM (2016) Neurite outgrowth is driven by actin polymerization even in the presence of actin polymerization inhibitors. *Mol Biol Cell* 27:3695–3704.
- Chen X, Wu X, Wu H, Zhang M (2020) Phase separation at the synapse. *Nat Neurosci* 23:301–310.
- Chorin E, Vinograd O, Fleidervish I, Gilad D, Herrmann S, Sekler I, Aizenman E, Hershinkel M (2011) Upregulation of KCC2 activity by zinc-mediated neurotransmission via the mZnR/GPR39 receptor. *J Neurosci* 31:12916–12926.
- Cohen I, Navarro V, Clemenceau S, Baulac M, Miles R (2002) On the origin of interictal activity in human temporal lobe epilepsy *in vitro*. *Science* 298:1418–1421.
- DeFazio RA, Keros S, Quick MW, Hablitz JJ (2000) Potassium-coupled chloride cotransport controls intracellular chloride in rat neocortical pyramidal neurons. *J Neurosci* 20:8069–8076.
- Delpire E, Staley KJ (2014) Novel determinants of the neuronal Cl⁻ concentration. *J Physiol* 592:4099–4114.
- Donnan FG (1911) The theory of membrane equilibrium in the presence of a non-dialyzable electrolyte. *Z Electrochem* 17:572–581.
- Doyon N, Vinay L, Prescott SA, De Koninck Y (2016) Chloride regulation: a dynamic equilibrium crucial for synaptic inhibition. *Neuron* 89:1157–1172.
- Duebel J, Haverkamp S, Schleich W, Feng G, Augustine GJ, Kuner T, Euler T (2006) Two-photon imaging reveals somatodendritic chloride gradient in retinal ON-type bipolar cells expressing the biosensor Clomeleon. *Neuron* 49:81–94.
- Düsterwald KM, Currin CB, Burman RJ, Akerman CJ, Kay AR, Raimondo JV (2018) Biophysical models reveal the relative importance of transporter proteins and impermeant anions in chloride homeostasis. *Elife* 7:e39575.
- Dyhrfeld-Johnsen J, Berdichevsky Y, Swiercz W, Sabolek H, Staley K (2010) Interictal spikes precede ictal discharges in an organotypic hippocampal slice culture model of epileptogenesis. *J Clin Neurophysiol* 27:418–424.
- Dzhala VI, Staley KJ (2020) KCC2 chloride transport contributes to the termination of ictal epileptiform activity. *eNeuro* 8:ENEURO.0208-20.2020.
- Dzhala VI, Talos DM, Sdrulla DA, Brumback AC, Mathews GC, Benke TA, Delpire E, Jensen FE, Staley KJ (2005) NKCC1 transporter facilitates seizures in the developing brain. *Nat Med* 11:1205–1213.
- Dzhala VI, Brumback AC, Staley KJ (2008) Bumetanide enhances phenobarbital efficacy in a neonatal seizure model. *Ann Neurol* 63:222–235.
- Dzhala VI, Kuchibhotla KV, Glykys JC, Kahle KT, Swiercz WB, Feng G, Kuner T, Augustine GJ, Bacskai BJ, Staley KJ (2010) Progressive NKCC1-

- dependent neuronal chloride accumulation during neonatal seizures. *J Neurosci* 30:11745–11761.
- Dzhala VI, Valeeva G, Glykys J, Khazipov R, Staley KJ (2012) Traumatic alterations in GABA signaling disrupt hippocampal network activity in the developing brain. *J Neurosci* 32:4017–4031.
- Fatin-Rouge N, Milon A, Buffle J, Goulet RR, Tessier A (2003) Diffusion and partitioning of solutes in agarose hydrogels: the relative influence of electrostatic and specific interactions. *J Phys Chem B* 107:12126–12137.
- Fenteany G, Zhu S (2003) Small-molecule inhibitors of actin dynamics and cell motility. *Curr Top Med Chem* 3:593–616.
- Földy C, Lee S-H, Morgan RJ, Soltesz I (2010) Regulation of fast-spiking basket cell synapses by the chloride channel ClC-2. *Nat Neurosci* 13:1047–1049.
- Galanopoulou AS (2008) Dissociated gender-specific effects of recurrent seizures on GABA signaling in CA1 pyramidal neurons: role of GABA_A receptors. *J Neurosci* 28:1557–1567.
- Garand D, Mahadevan V, Woodin MA (2019) Ionotropic and metabotropic kainate receptor signalling regulates Cl⁻ homeostasis and GABAergic inhibition. *J Physiol* 597:1677–1690.
- Gianazza E, Righetti PG (1980) Size and charge distribution of macromolecules in living systems. *J Chromatogr A* 193:1–8.
- Gillen CM, Brill S, Payne JA, Forbush B (1996) Molecular cloning and functional expression of the K-Cl cotransporter from rabbit, rat, and human: a new member of the cation-chloride cotransporter family. *J Biol Chem* 271:16237–16244.
- Glykys J, Dzhala VI, Kuchibhotla KV, Feng G, Kuner T, Augustine G, Bacskai BJ, Staley KJ (2009) Differences in cortical versus subcortical GABAergic signaling: a candidate mechanism of electroclinical uncoupling of neonatal seizures. *Neuron* 63:657–672.
- Glykys J, Dzhala V, Egawa K, Balena T, Saponjian Y, Kuchibhotla K, Bacskai B, Kahle K, Zeuthen T, Staley K (2014a) Local impermeant anions establish the neuronal chloride concentration. *Science* 343:670–675.
- Glykys J, Dzhala V, Egawa K, Balena T, Saponjian Y, Kuchibhotla K, Bacskai B, Kahle K, Zeuthen T, Staley K (2014b) Response to comments on “Local impermeant anions establish the neuronal chloride concentration.” *Science* 345:1130.
- Glykys J, Dzhala V, Egawa K, Kahle KT, Delpire E, Staley K (2017) Chloride dysregulation, seizures, and cerebral edema: a relationship with therapeutic potential. *Trends Neurosci* 40:276–294.
- Glykys J, Duquette E, Rahmati N, Duquette K, Staley K (2019) Mannitol decreases neocortical epileptiform activity during early brain development via cotransport of chloride and water. *Neurobiol Dis* 125:163–175.
- Golmohamadi M, Davis TA, Wilkinson KJ (2012) Diffusion and partitioning of cations in an agarose hydrogel. *J Phys Chem A* 116:6505–6510.
- Goutierre M, Al Awabdh S, Donneger F, François E, Gomez-Dominguez D, Irinopoulou T, de la Prida LM, Poncer JC (2019) KCC2 regulates neuronal excitability and hippocampal activity via interaction with Task-3 channels. *Cell Rep* 28:91–103.e7.
- Gregor HP (1951) Gibbs-Donnan equilibria in ion exchange resin systems. *J Am Chem Soc* 73:642–650.
- Grienberger C, Milstein AD, Bittner KC, Romani S, Magee JC (2017) Inhibitory suppression of heterogeneously tuned excitation enhances spatial coding in CA1 place cells. *Nat Neurosci* 20:417–426.
- Grimley JS, Li L, Wang W, Wen L, Beese LS, Hellinga HW, Augustine GJ (2013) Visualization of synaptic inhibition with an optogenetic sensor developed by cell-free protein engineering automation. *J Neurosci* 33:16297–16309.
- Gulledge AT, Stuart GJ (2003) Excitatory actions of GABA in the cortex. *Neuron* 37:299–309.
- Gut G, Herrmann MD, Pelkmans L (2018) Multiplexed protein maps link subcellular organization to cellular states. *Science* 361:eaar7042.
- Helferich FG (1995) Ion exchange. New York: Dover.
- Heubl M, Zhang J, Pressey JC, Al Awabdh S, Renner M, Gomez-Castro F, Moutkine I, Eugène E, Russeau M, Kahle KT, Poncer JC, Lévi S (2017) GABA A receptor dependent synaptic inhibition rapidly tunes KCC2 activity via the Cl⁻-sensitive WNK1 kinase. *Nat Commun* 8:1776.
- Hübner CA, Stein V, Hermans-Borgmeyer I, Meyer T, Ballanyi K, Jentsch TJ (2001) Disruption of KCC2 reveals an essential role of K-Cl cotransport already in early synaptic inhibition. *Neuron* 30:515–524.
- Huguenard J, Alger B (1986) Whole-cell voltage-clamp study of the fading of GABA-activated currents in acutely dissociated hippocampal neurons. *J Neurophysiol* 56:1–18.
- Ilie A, Raimondo JV, Akerman CJ (2012) Adenosine release during seizures attenuates GABA_A receptor-mediated depolarization. *J Neurosci* 32:5321–5332.
- Jacob T, Lillis KP, Wang Z, Swiercz W, Rahmati N, Staley KJ (2019) A proposed mechanism for spontaneous transitions between interictal and ictal activity. *J Neurosci* 39:557–575.
- Janke C, Rogowski K, Van Dijk J (2008) Polyglutamylation: a fine-regulator of protein function? *EMBO Rep* 9:636–641.
- Jarolimek W, Lewen A, Misgeld U (1999) A furosemide-sensitive K⁺-Cl⁻ cotransporter counteracts intracellular Cl⁻ accumulation and depletion in cultured rat midbrain neurons. *J Neurosci* 19:4695–4704.
- Jin X, Huguenard JR, Prince DA (2005) Impaired Cl⁻ extrusion in layer V pyramidal neurons of chronically injured epileptogenic neocortex. *J Neurophysiol* 93:2117–2126.
- Kahle KT, Khanna AR, Alper SL, Adragna NC, Lauf PK, Sun D, Delpire E (2015) K-Cl cotransporters, cell volume homeostasis, and neurological disease. *Trends Mol Med* 21:513–523.
- Khazipov R (2016) GABAergic synchronization in epilepsy. *Cold Spring Harb Perspect Med* 6:a022764.
- Khirurg S, Huttu K, Ludwig A, Smirnov S, Voipio J, Rivera C, Kaila K, Khiroug L (2005) Distinct properties of functional KCC2 expression in immature mouse hippocampal neurons in culture and in acute slices. *Eur J Neurosci* 21:899–904.
- Khirurg S, Yamada J, Afzalov R, Voipio J, Khiroug L, Kaila K (2008) GABAergic depolarization of the axon initial segment in cortical principal neurons is caused by the Na-K-2Cl cotransporter NKCC1. *J Neurosci* 28:4635–4639.
- Kim C-H, Lisman JE (1999) A role of actin filament in synaptic transmission and long-term potentiation. *J Neurosci* 19:4314–4324.
- Köhling R, Vreugdenhil M, Bracci E, Jefferys JG (2000) Ictal epileptiform activity is facilitated by hippocampal GABA_A receptor-mediated oscillations. *J Neurosci* 20:6820–6829.
- Koleske AJ (2013) Molecular mechanisms of dendrite stability. *Nat Rev Neurosci* 14:536–550.
- Krapf R, Berry C, Verkman A (1988) Estimation of intracellular chloride activity in isolated perfused rabbit proximal convoluted tubules using a fluorescent indicator. *Biophys J* 53:955–962.
- Krishnan GP, Bazhenov M (2011) Ionic dynamics mediate spontaneous termination of seizures and postictal depression state. *J Neurosci* 31:8870–8882.
- Kuner T, Augustine GJ (2000) A genetically encoded ratiometric indicator for chloride. *Neuron* 27:447–459.
- Lagostena L, Rosato-Siri M, D’Onofrio M, Brandi R, Arisi I, Capsoni S, Franzot J, Cattaneo A, Cherubini E (2010) In the adult hippocampus, chronic nerve growth factor deprivation shifts GABAergic signaling from the hyperpolarizing to the depolarizing direction. *J Neurosci* 30:885–893.
- Lee HH, Jurd R, Moss SJ (2010) Tyrosine phosphorylation regulates the membrane trafficking of the potassium chloride co-transporter KCC2. *Mol Cell Neurosci* 45:173–179.
- Lillis KP, Kramer MA, Mertz J, Staley KJ, White JA (2012) Pyramidal cells accumulate chloride at seizure onset. *Neurobiol Dis* 47:358–366.
- Luhmann HJ, Kirischuk S, Kilb W (2014) Comment on “Local impermeant anions establish the neuronal chloride concentration.” *Science* 345:1130–1130.
- MacKenzie G, Maguire J (2015) Chronic stress shifts the GABA reversal potential in the hippocampus and increases seizure susceptibility. *Epilepsy Research* 109:13–27.
- Maccferri G, David J, Roberts B, Szucs P, Cottingham CA, Somogyi P (2000) Cell surface domain specific postsynaptic currents evoked by identified GABAergic neurones in rat hippocampus in vitro. *J Physiol* 524:91–116.
- Manning GS (1978) The molecular theory of polyelectrolyte solutions with applications to the electrostatic properties of polynucleotides. *Q Rev Biophys* 11:179–246.
- Marinsky JA (1985) An interpretation of the sensitivity of weakly acidic (basic) polyelectrolyte (cross-linked and linear) equilibria to excess neutral salt. *J Phys Chem* 89:5294–5302.
- Marinsky J (1993) A Gibbs-Donnan-based analysis of ion-exchange and related phenomena. In: Ion exchange and solvent extraction (Marinsky JA, Marcus Y, eds). Marcel Dekker: New York.
- Masuda T, Dobson GP, Veech RL (1990) The Gibbs-Donnan near-equilibrium system of heart. *J Biol Chem* 265:20321–20334.

- Morawski M, Reinert T, Meyer-Klaucke W, Wagner FE, Tröger W, Reinert A, Jäger C, Brückner G, Arendt T (2015) Ion exchanger in the brain: quantitative analysis of perineuronally fixed anionic binding sites suggests diffusion barriers with ion sorting properties. *Sci Rep* 5:16471.
- Morton WM, Ayscough KR, McLaughlin PJ (2000) Latrunculin alters the actin-monomer subunit interface to prevent polymerization. *Nat Cell Biol* 2:376–378.
- Nakahata Y, Miyamoto A, Watanabe M, Moorhouse AJ, Nabekura J, Ishibashi H (2010) Depolarizing shift in the GABA-induced current reversal potential by lidocaine hydrochloride. *J Brain Research* 1345:19–27.
- Ormond J, Woodin MA (2009) Disinhibition mediates a form of hippocampal long-term potentiation in area CA1. *PLoS One* 4:e7224.
- Pavlov I, Scimemi A, Savtchenko L, Kullmann DM, Walker MC (2011) I_h-mediated depolarization enhances the temporal precision of neuronal integration. *Nature Communications* 2:1–9.
- Pouzat C, Marty A (1999) Somatic recording of GABAergic autoreceptor current in cerebellar stellate and basket cells. *J Neurosci* 19:1675–1690.
- Procter HR (1914) XXXV.—The equilibrium of dilute hydrochloric acid and gelatin. *J Chem Soc Trans* 105:313–327.
- Rahmati N, Veloz MFV, Xu J, Barone S, Hamida NRB, Schonewille M, Hoebeek FE, Soleimani M, De Zeeuw CI (2016) SLC26A11 (KBAT) in Purkinje cells is critical for inhibitory transmission and contributes to locomotor coordination. *eNeuro* 3:ENEURO.0028-16.2016.
- Raimondo JV, Richards BA, Woodin MA (2017) Neuronal chloride and excitability—the big impact of small changes. *Curr Opin Neurobiol* 43:35–42.
- Rial Verde E, Zayat L, Etchenique R, Yuste R (2008) Photorelease of GABA with visible light using an inorganic caging group. *Front Neural Circuits* 2:2.
- Riekkki R, Pavlov I, Tornberg J, Lauri SE, Airaksinen MS, Taira T (2008) Altered synaptic dynamics and hippocampal excitability but normal long-term plasticity in mice lacking hyperpolarizing GABA_A receptor-mediated inhibition in CA1 pyramidal neurons. *J Neurophysiol* 99:3075–3089.
- Rinke I, Artmann J, Stein V (2010) ClC-2 voltage-gated channels constitute part of the background conductance and assist chloride extrusion. *J Neurosci* 30:4776–4786.
- Romijn H, De Jong B, Ruijter J (1988) A procedure for culturing rat neocortex explants in a serum-free nutrient medium. *J Neurosci Methods* 23:75–83.
- Romo-Parra H, Treviño M, Heinemann U, Gutiérrez R (2008) GABA actions in hippocampal area CA3 during postnatal development: differential shift from depolarizing to hyperpolarizing in somatic and dendritic compartments. *J Neurophysiol* 99:1523–1534.
- Sanabria H, Miller JH Jr, Mershin A, Luduena RF, Kolomenski AA, Schuessler HA, Nanopoulos DV (2006) Impedance spectroscopy of α - β tubulin heterodimer suspensions. *Biophys J* 90:4644–4650.
- Sato SS, Artoni P, Landi S, Cozzolino O, Parra R, Pracucci E, Trovato F, Szczurkowska J, Luin S, Arosio D, Beltram F, Cancedda L, Kaila K, Ratto GM (2017) Simultaneous two-photon imaging of intracellular chloride concentration and pH in mouse pyramidal neurons in vivo. *Proc Natl Acad Sci U S A* 114:E8770–E8779.
- Sauer JF, Strüber M, Bartos M (2012) Interneurons provide circuit-specific depolarization and hyperpolarization. *J Neurosci* 32:4224–4229.
- Savtchenko LP, Poo MM, Rusakov DA (2017) Electrodiffusion phenomena in neuroscience: a neglected companion. *Nat Rev Neurosci* 18:598–612.
- Schmidt T, Ghaffarian N, Philippot C, Seifert G, Steinhäuser C, Pape H-C, Blaesse P (2018) Differential regulation of chloride homeostasis and GABAergic transmission in the thalamus. *Sci Rep* 8:13929.
- Silayeva L, Deeb TZ, Hines RM, Kelley MR, Munoz MB, Lee HHC, Brandon NJ, Dunlop J, Maguire J, Davies PA, Moss SJ (2015) KCC2 activity is critical in limiting the onset and severity of status epilepticus. *Proc Natl Acad Sci U S A* 112:3523–3528.
- Sipilä ST, Huttu K, Yamada J, Afzalov R, Voipio J, Blaesse P, Kaila K (2009) Compensatory enhancement of intrinsic spiking upon NKCC1 disruption in neonatal hippocampus. *J Neurosci* 29:6982–6988.
- Sivakumaran S, Cardarelli RA, Maguire J, Kelley MR, Silayeva L, Morrow DH, Mukherjee J, Moore YE, Mather RJ, Duggan ME, Brandon NJ, Dunlop J, Zicha S, Moss SJ, Deeb TZ (2015) Selective inhibition of KCC2 leads to hyperexcitability and epileptiform discharges in hippocampal slices and *in vivo*. *J Neurosci* 35:8291–8296.
- Sola M, Kneussel M, Heck IS, Betz H, Weissenhorn W (2001) X-ray crystal structure of the trimeric N-terminal domain of gephyrin. *J Biol Chem* 276:25294–25301.
- Somogyi P, Nunzi M, Gorio A, Smith A (1983) A new type of specific interneuron in the monkey hippocampus forming synapses exclusively with the axon initial segments of pyramidal cells. *Brain Res* 259:137–142.
- Spruston N, Stuart G, Häusser M (2016) Principles of dendritic integration. In: *Dendrites* (Stuart G, Spruston N, Häusser M, eds), pp 351–398. Oxford, UK: Oxford UP.
- Staley KJ, Mody I (1992) Shunting of excitatory input to dentate gyrus granule cells by a depolarizing GABA_A receptor-mediated postsynaptic conductance. *J Neurophysiol* 68:197–212.
- Staley KJ, Proctor WR (1999) Modulation of mammalian dendritic GABA_A receptor function by the kinetics of Cl⁻ and HCO₃⁻ transport. *J Physiol* 519:693–712.
- Staley KJ, Soldo BL, Proctor WR (1995) Ionic mechanisms of neuronal excitation by inhibitory GABA_A receptors. *Science* 269:977–981.
- Stein V, Hermans-Borgmeyer I, Jentsch TJ, Hübner CA (2004) Expression of the KCl cotransporter KCC2 parallels neuronal maturation and the emergence of low intracellular chloride. *J Comp Neurol* 468:57–64.
- Stoppini L, Buchs P-A, Müller D (1991) A simple method for organotypic cultures of nervous tissue. *J Neurosci Methods* 37:173–182.
- Szabadics J, Varga C, Molnár G, Oláh S, Barzó P, Tamás G (2006) Excitatory effect of GABAergic axo-axonic cells in cortical microcircuits. *Science* 311:233–235.
- Tanaka T, Saito H, Matsuki N (1997) Inhibition of GABA_A synaptic responses by brain-derived neurotrophic factor (BDNF) in rat hippocampus. *J Neurosci* 17:2959–2966.
- Thompson SM, Deisz RA, Prince DA (1988) Relative contributions of passive equilibrium and active transport to the distribution of chloride in mammalian cortical neurons. *J Neurophysiol* 60:105–124.
- Tyzio R, Holmes GL, Ben-Ari Y, Khazipov R (2007) Timing of the developmental switch in GABA_A mediated signaling from excitation to inhibition in CA3 rat hippocampus using gramicidin perforated patch and extracellular recordings. *Epilepsia* 48:96–105.
- Tyzio R, Minlebaev M, Rheims S, Ivanov A, Jorquera I, Holmes GL, Zilberter Y, Ben-Ari Y, Khazipov R (2008) Postnatal changes in somatic γ -aminobutyric acid signalling in the rat hippocampus. *Eur J Neurosci* 27:2515–2528.
- Untiet V, Moeller LM, Ibarra-Soria X, Sánchez-Andrade G, Stricker M, Neuhaus EM, Logan DW, Gensch T, Spehr M (2016) Elevated cytosolic Cl⁻ concentrations in dendritic knobs of mouse vomeronasal sensory neurons. *Chem Senses* 41:669–676.
- Veech RL, Kashiwaya Y, Gates DN, King MT, Clarke K (2002) The energetics of ion distribution: the origin of the resting electric potential of cells. *IUBMB Life* 54:241–252.
- Verkman A, Sellers M, Chao A, Leung T, Ketcham R (1989) Synthesis and characterization of improved chloride-sensitive fluorescent indicators for biological applications. *Anal Biochem* 178:355–361.
- Voipio J, Kaila K (2000) GABAergic excitation and K⁺-mediated volume transmission in the hippocampus. In: *Progress in brain research*, pp 329–338. Amsterdam: Elsevier.
- Watanabe N, Mitchison TJ (2002) Single-molecule speckle analysis of actin filament turnover in lamellipodia. *Science* 295:1083–1086.
- Yamamoto S, Nakanishi K, Matsuno R (1988) Ion-exchange chromatography of proteins. Boca Raton, FL: CRC.
- Yang B, Rajput PS, Kumar U, Sastry BR (2015) Regulation of GABA equilibrium potential by mGluRs in rat hippocampal CA1 neurons. *PLoS one* 10:e0138215.
- Zhan RZ, Nadler JV, Schwartz-Bloom RD (2006) Depressed responses to applied and synaptically-released GABA in CA1 pyramidal cells, but not in CA1 interneurons, after transient forebrain ischemia. *J Cereb Blood Flow Metab* 26:112–124.
- Zorrilla de San Martín J, Trigo FF, Kawaguchi SY (2017) Axonal GABA_A receptors depolarize presynaptic terminals and facilitate transmitter release in cerebellar Purkinje cells. *J Physiol* 595:7477–7493.